Thermal conduction phenomena in carbon nanotubes and related nanostructured materials

Amy M. Marconnet,* Matthew A. Panzer,† and Kenneth E. Goodson‡

Department of Mechanical Engineering, Stanford University, Stanford, California 94305, USA

(published 16 August 2013)

The extremely high thermal conductivities of carbon nanotubes have motivated a wealth of research. Progress includes innovative conduction metrology based on microfabricated platforms and scanning thermal probes as well as simulations exploring phonon dispersion and scattering using both transport theory and molecular dynamics. This article highlights these advancements as part of a detailed review of heat conduction research on both individual carbon nanotubes and nanostructured films consisting of arrays of nanotubes or disordered nanotube mats. Nanotube length, diameter, and chirality strongly influence the thermal conductivities of individual nanotubes and the transition from primarily diffusive to ballistic heat transport with decreasing temperature. A key experimental challenge, for both individual nanotubes and aligned films, is the separation of intrinsic and contact resistances. Molecular dynamics simulations have studied the impacts of specific types of imperfections on the nanotube conductance and its variation with length and chirality. While the properties of aligned films fall short of predictions based on individual nanotube data, improvements in surface engagement and postfabrication nanotube quality are promising for a variety of applications including mechanically compliant thermal contacts.

DOI: 10.1103/RevModPhys.85.1295 PACS numbers: 65.80.−g, 61.48.De, 63.22.Gh

CONTENTS

*Present address: School of Mechanical Engineering, Purdue University, 585 Purdue Mall, West Lafayette, IN 47907, USA. amarconn@purdue.edu
†Present address: KLA-Tencor Corporation, 1 Technology Drive, Milpitas, CA 95035, USA.
‡goodson@stanford.edu

I. INTRODUCTION

Carbon nanotubes (CNTs) are promising for applications leveraging their unique electrical, thermal, and mechanical properties. Early predictions and measurements (Overney, Zhong, and Tománek, 1993; Treacy, Ebbesen, and Gibson, 1996) suggested extremely high mechanical strength and strength-to-weight ratio. Nanotubes can be metallic or semiconducting based on their chirality and diameter leading to a wealth of research on CNT-based nanoelectronic devices (Dresselhaus, Dresselhaus, and Saito, 1995). High expectations for the thermal conductivity of CNTs were originally based on the high in-plane thermal conductivity of graphite and the high thermal conductivity of bulk and thin film diamond (Ruoff and Lorents, 1995). Molecular dynamics (MD) simulations (Berber, Kwon, and Tománek, 2000) predicted thermal conductivities as high as 6600 $\mathrm{W\,m^{-1}\,K^{-1}}$ at room temperature. These findings motivated exploratory research for a wide variety of applications including reinforced composites (Thostenson, Ren, and Chou, 2001), field emission devices (Baughman, Zakhidov, and de Heer, 2002), sensors and probes (Baughman, Zakhidov, and de Heer, 2002), and thermal interface materials (K. Zhang *et al.*, 2005).

This review provides a comprehensive overview of thermal conduction research on carbon nanotubes and nanostructured films consisting of arrays of nanotubes or disordered nanotube mats with a focus on understanding the trends with geometrical parameters and the differences between predictions and data. For individual nanotubes, the problem of comparing data from differing groups is addressed by calculating thermal conductivities using a consistent definition of

the cross-sectional area. For films containing aligned carbon nanotubes, the relatively low conductivities reported experimentally compared to the original prediction from individual nanotube data are discussed considering individual nanotube data and issues associated with CNT film fabrication and mechanical attachment. The highly productive period of research covered by this review has enriched the discipline of heat conduction with a variety of novel microelectromechanical systems-based experimental methods and opportunities for calibration and validation of molecular dynamics simulations. In addition to covering the properties of nanotubes and related nanostructured materials, this review discusses these new experimental methodologies and their implications for future research.

This review fills an important gap in the literature already available on carbon nanotubes, which at present lacks a comprehensive, comparative review of the extensive and sometimes revolutionary experimental and theoretical research addressing this material system. Several articles [e.g., Dresselhaus, Dresselhaus, and Saito (1995)] and at least one book [e.g., Dresselhaus, Dresselhaus, and Avouris (2001)] detailed the structure and synthesis of carbon nanotubes. Early reviews of CNT properties (Dresselhaus *et al.*, 2004; Dresselhaus, Dresselhaus, and Jorio, 2004; Mamalis, Vogtländer, and Markopoulos, 2004; Dresselhaus, Dresselhaus, and Hofmann, 2008; Eletskii, 2009) discussed thermal transport but did not attempt a comprehensive comparison of data and predictions. Hone (2001, 2004) provided insightful summaries of the theoretical and experimental progress on CNT thermal transport, just a few years after the first experimental data were available. In the years since those reviews, rather substantial progress has been made in both theory and experiments, including approximately 75 additional articles cited in this paper. Lee *et al.* (2010) reviewed molecular dynamics simulations of thermal conduction along single-wall carbon nanotubes (SWCNTs) and examined variations with nanotube length, chirality, and temperature. Balandin (2011) reviewed thermal transport in many forms of nanoscale carbon materials from amorphous carbon to CNTs with an emphasis on graphene and the unique characteristics of two-dimensional (2D) crystals. There remains a need for a more complete comparison of predictions and experimental data for individual nanotubes with a focus on identifying both the resolved issues and the open questions. Furthermore, the maturing body of literature on nanotube-based films, when considered together with extrapolations of the data reviewed here for individual nanotubes, provides a compelling chance to examine the physical mechanisms that may be limiting the thermal conductance of nanotube ensembles. In addition to discussing and interpreting the research results, this review also highlights the rich variety of innovative methods, for both experiments and simulations, that has been developed for CNT thermal transport studies.

This paper includes separate sections on individual nanotubes and films, each of which includes sections addressing theory and experimental methods. Section II focuses on individual nanotubes including theoretical modeling and measurements. Section III extends the discussion to nanotube films, focusing mainly on aligned arrays of nanotubes. Section IV focuses on the use of CNT and CNT-based films in practical applications.

II. THERMAL CONDUCTION BY INDIVIDUAL NANOTUBES

A. Physical mechanisms

The unusual properties of carbon nanotubes are governed by their unusual and simple atomic structure, which has been examined in a variety of chiralities and diameters. Comparison of the theoretical results and experimental data in the literature is complicated by the variety of nanotubes produced by different techniques.

A single-wall carbon nanotube consists of an atomic layer of carbon atoms (i.e., a sheet of graphene) rolled into the form of a tube. The axis of the nanotube can form along many different directions [i.e., chiral vectors (n, m)] in the carbon layer, yielding CNTs with different chiralities and diameters. Armchair (n, n) nanotubes are always metallic, while zigzag $(n, 0)$ and other (n, m) chiralities are semiconducting (Dresselhaus, Dresselhaus, and Jorio, 2004). Multiwall carbon nanotubes (MWCNTs) include several concentric tubes that can have varying chiralities, and understanding the interactions between shells is critical for accurate modeling of thermal transport.

Heat conduction by carbon nanotubes is dominated by the coupled vibrations of carbon atoms and therefore can be analyzed as phonon transport. Phonon transport dominates over heat conduction by electrons even in those nanotube chiralities that exhibit metallic properties (Hone, 2001; Balandin, 2011). The phonon dispersion relationship [see Fig. 2(b)] consists of four acoustic modes (one longitudinal mode, two transverse modes, and one torsional or "twist" mode) and many optical modes. The twist acoustic mode arises from torsion of the tube about its axis, which can be described as a twisting motion (Dresselhaus and Eklund, 2000). The phonon conductivity can be computed from the phonon dispersion relationship, the heat capacity of each phonon mode, and their scattering rates or mean free paths. The Debye temperature is expected to be significantly higher than room temperature (Huang *et al.*, 2011) and likely similar to graphene, graphite, and diamond [2500 K (Maruyama, 2003; Dresselhaus *et al.*, 2004)]. Therefore even at room temperature the heat capacity and, thus, thermal conductivity are impacted by quantum effects (Li, 2000; Maruyama, 2003; Zhong and Lukes, 2004).

Carbon nanotubes and other low-dimensional carbon-based nanomaterials including graphene can have very high thermal conductivities, despite very small cross-sectional dimensions. This is in contrast to many crystalline nanowires with small cross-sectional dimensions in which the thermal conductivity is strongly reduced by the increased rate of phonon-boundary scattering. The long range crystallinity, long phonon mean free path, and large speed of sound of the CNTs lead to the large thermal conductivity (Dresselhaus, Dresselhaus, and Jorio, 2004). For ideal perfect three-dimensional crystals, lattice anharmonicity limits thermal conduction. However, for low-dimensional structures, the intrinsic thermal conductivities of ideal one-dimensional (1D) and two-dimensional systems diverge with the number of atoms leading to infinite intrinsic thermal conductivity despite anharmonicity (Balandin, 2011). Practically, the thermal conductivities of 1D and 2D systems are limited by many factors including higher-order phonon

scattering processes (Mingo and Broido, 2005b; Wang, Tang, Zheng *et al.*, 2007), sample quality (i.e., defects and impurities), and boundary scattering.

The phonon mean free path in carbon nanotubes depends on phonon-phonon, phonon-boundary, and phonon-defect scattering processes (see Sec. II.D.3). Estimates of the phonon mean free path at room temperature range from about 50 nm (Choi *et al.*, 2006) to 1.5 μm (Hone *et al.*, 1999; Yamamoto, Watanabe, and Watanabe, 2004a), although MWCNTs with many defects may have phonon mean free paths as small as 4 nm (Pettes and Shi, 2009). The dominant phonon wavelength λ_d for heat transport can be estimated from $\hbar v/\lambda_d \approx k_B T$, where $\hbar = h/2\pi$, h is Planck's constant, v is the phonon velocity, k_B is the Boltzmann constant, and T is the temperature (Prasher, Tong, and Majumdar, 2007). For SWCNTs, the large phonon velocity predicts a large dominant phonon wavelength even at moderately high temperatures (Prasher, Tong, and Majumdar, 2007).

A challenge with interpreting the existing theory and data is the transition from the ballistic to the diffusive conduction regimes. In the ballistic regime, phonons scatter rarely along the length of the nanotube, and thus the thermal conductance is independent of nanotube length. Thus, carbon nanotubes are ballistic conductors when the mean free path is longer than the nanotube length and the dominant phonon wavelength is smaller than the nanotube diameter. At very low temperatures (a few Kelvin), only the four acoustic modes contribute to heat transfer and as the temperature increases the optical modes begin to contribute. In the diffusive regime, phonons scatter many times within the length of the nanotube. Diffusive heat transport dominates when the CNT is much longer than both the phonon mean free path and the dominant phonon wavelength. Thermal conduction within carbon nanotubes transitions from the ballistic to diffusive regime with increasing temperature (see Sec. II.D.2) or increasing length (see Sec. II.D.1).

Another challenge faced by this review is the distinction between the thermal conductance G and the thermal conductivity k. The thermal conductance simply quantifies the rate of heat transferred q for a given temperature rise ΔT by means of $G = q/\Delta T$. The thermal conductivity is defined from Fourier's law for diffusive thermal transport by means of $q = -kAdT/dx$, where q is the heat flux, A is the cross-sectional area, and dT/dx is the temperature gradient along the length of the nanotube. The thermal conductivity and thermal conductance are related through geometrical parameters by $G = kA/L$, where L is the length of the nanotube. The thermal resistance R at an interface is defined as the temperature rise across the interface due to a heat flux $R = \Delta T/q$.

While the conductance is well defined for a given CNT sample, the precise meaning of the thermal conductivity relies on the definition of the cross-sectional area. Several definitions and considerable ambiguity have resulted from the annular geometry of the tube, some ambiguity of the cross-sectional area of an individual atomic layer, especially in a SWCNT, and the challenges in measuring the inner diameter of MWCNTs. Typical definitions are (1) the whole area enclosed by the outermost tube of carbon atoms [e.g., Fujii *et al.* (2005)] or (2) the approximate area of the carbon atoms in CNT [e.g., Yu *et al.* (2005)]. For SWCNTs, this second method is often approximated as the circumference of the CNT multiplied by the thickness of the carbon shell, which is typically chosen to be between the sp^2 bond length ($\delta = 0.142$ nm) and the interlayer spacing in graphite ($\delta = 0.34$ nm) (Yao *et al.*, 2005). For a single value of the nanotube thermal conductance, two different values of thermal conductivity can be extracted. Note that for (10,10) SWCNTs (1.35 nm diameter), both definitions of area are consistent to within 1% when assuming a carbon thickness of $\delta = 0.34$ nm. This paper standardizes the thermal conductivities reported by different authors using the first definition of cross-sectional area (1), which is the entire enclosed area, which is necessitated by the fact that few experimental papers reported inner MWCNT diameters.

B. Experimental progress

Measurements of thermal properties of individual CNTs usually require microfabricated devices and can be separated into two groups: (1) experiments using an external heat source to establish a temperature gradient across the nanotubes, and (2) experiments using self-heating of the nanotube to extract the thermal properties (see Fig. 1).

Table I summarizes the available experimental data for the thermal conductivity of individual nanotubes. Using the external heating method, both Kim *et al.* (2001) and Yu *et al.* (2005) measured the thermal conductivity of a 2.5 μm long, 14 nm diameter MWCNT and a 2.76 μm long, 1–3 nm diameter SWCNT, respectively, by suspending the nanotubes between two resistive elements. Heat generated at one resistor flowed in part through the nanotube and was detected through a temperature rise at the second. Both resistors served as temperature sensors and the nanotube conductance was calculated considering losses through the support legs. As discussed later, a challenge with this method is isolating the conductance internal to the nanotube from the thermal resistances at the interfaces with the heating and sensing elements. For bundles of nanotubes similarly suspended between two resistive elements, the sensitivity to thermal conductivity was improved when using sinusoidal heating and lock-in detection of the voltage signals (Shi *et al.*, 2003). Using this method, Pettes and Shi (2009) measured the thermal conductivity of several SWCNTs and MWCNTs. A similar external heating method was used by Fujii *et al.* (2005) with a T-type nanosensor (Zhang, Fujiwara, and Fujii, 1999) to measure the thermal conductivity of three MWCNTs ranging from 9.8 to 28.2 nm in diameter and 1.89 to 3.7 μm in length. Each CNT was connected from the center of a hot bridge to a heat sink. A lower bound for the thermal conductivity of the nanotube was extracted from the measured temperatures and heat generation rates neglecting contact resistance of the nanotube and the hot wire and heat sink.

Methods for extracting thermal information using self-heating of the nanotube include calibrating the thermal coefficient of resistance (Pop *et al.*, 2006), the 3ω technique (Choi *et al.*, 2005, 2006; Wang, Tang, Zheng *et al.*, 2007; Wang, Tang, Li *et al.*, 2007), and Raman observation of the

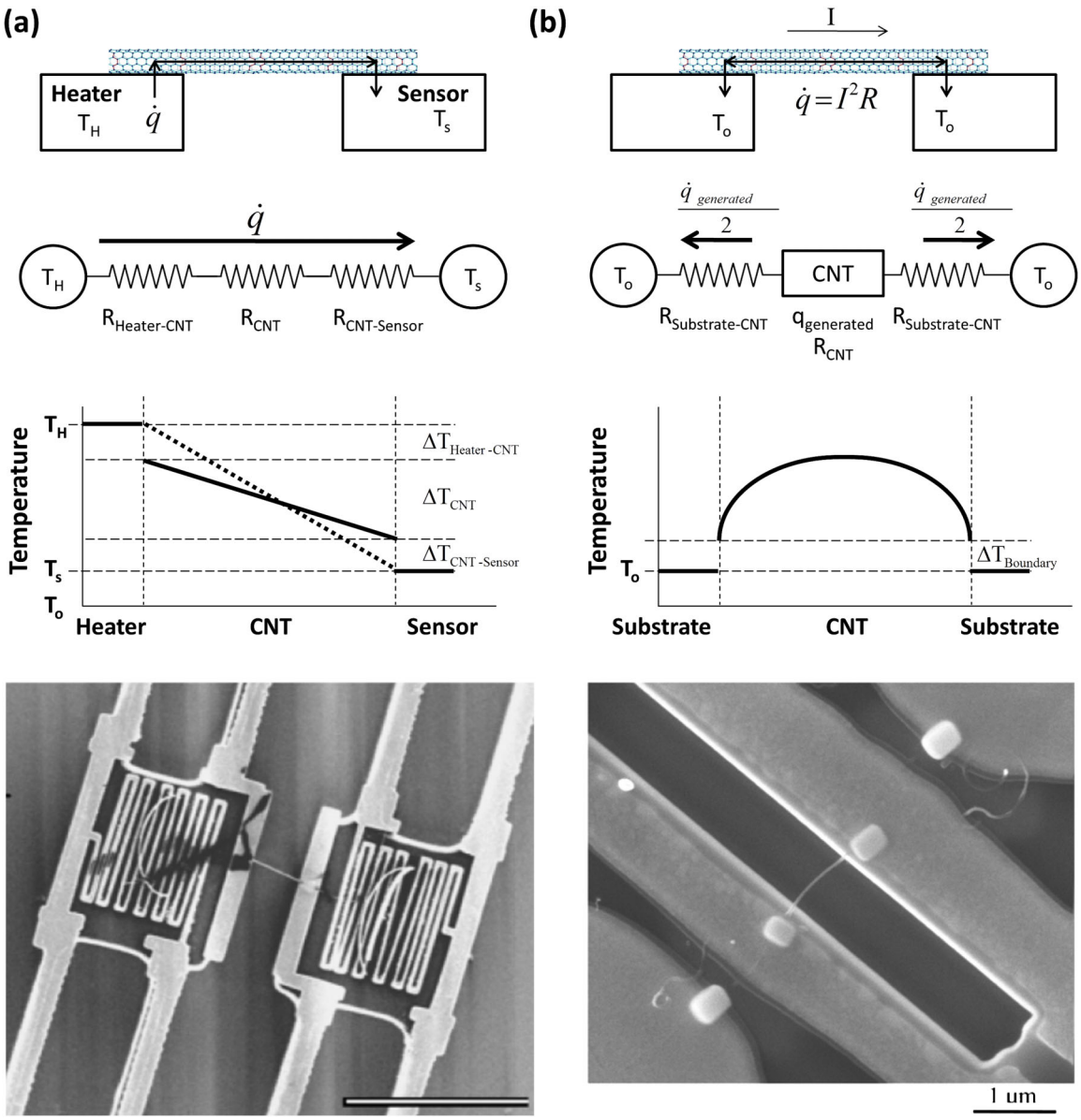

FIG. 1 (color online). Two differing strategies for measuring thermal conductivity of individual carbon nanotubes. (a) Passive technique. A temperature difference generated by a heater at one end of the nanotube is captured using sensors at both ends. This SEM image is taken from Kim *et al.* (2001) and depicts a measurement setup consisting of an individual MWCNT suspended between two resistive elements. The scale bar represents 10 μm. (b) Self-heating technique. Heat is generated by applying a voltage across the nanotube, resulting in electrical heating of the nanotube, and the temperature distribution is deduced from the resulting electrical resistance change and calibration data. SEM image of a four-point 3ω setup for a MWCNT. From Choi *et al.*, 2006.

temperature profile (Li *et al.*, 2009). Pop *et al.* (2006) measured the *I-V* characteristics of a self-heated CNT suspended across a trench to extract the thermal conductivity as a function of temperature. Choi *et al.* (2005, 2006), Wang, Tang, Zheng *et al.* (2007), and Wang, Tang, Li *et al.* (2007) used the 3ω technique (Cahill, 1990) to determine the thermal conductivity of nanotubes from 0.509 to 6.941 μm long. A novel technique by Li *et al.* (2009) combined electrical self-heating of a nanotube with temperature measurements using the Raman shift method. Previously, Hsu *et al.* (2008) used laser heating of the nanotube and the Raman shift method for measuring the temperature profile along the nanotube to extract information about the relative contribution of the intrinsic thermal resistance of the nanotube and the boundary resistance between the nanotube and the substrate. Since the exact magnitude of optical power absorbed by the nanotube was unknown, the thermal conductivity of the sample could not be determined. To address this challenge, Li *et al.* (2009) combined electrical self-heating of the nanotube with temperature measurements via the Raman shift method. The shape of the temperature profile along the nanotube axis depends only on the intrinsic thermal conductivity allowing determination of the thermal conductivity independent of boundary resistance. A large portion of the CNT was in contact with the substrate and the thermal contact resistance at the ends of the nanotube was small compared to the intrinsic resistance of the nanotube.

TABLE I. Measured room temperature thermal conductivities of individual carbon nanotubes. Data from all authors are standardized here using the enclosed cross-sectional area of the nanotube (i.e., using the outside diameter for MWCNTs). Additionally, for SWCNT samples, the thermal conductivity calculated with the circumference times the thickness of a nanotube shell is shown for comparison. Yu *et al.* (2005) measured the thermal conductance and uncertainty in the diameter of the nanotube resulted in a wide range for the thermal conductivity. Pettes and Shi (2009) reported a lower bound in thermal conductivity for SWCNT and double-wall carbon nanotubes (DWCNTs), but extracted an estimate of the intrinsic thermal conductivity for the MWCNTs. Choi *et al.* (2005, 2006) did not explicitly state which definition of area they used to calculate thermal conductivity, so the value in the table is as reported in the articles.

Article	Measurement technique	SWCNT MWCNT	Length (μm)	Diameter (nm)	k^a (W m^{-1} K^{-1})	k'^b (W m^{-1} K^{-1})	Boundary resistance
Yu *et al.* (2005)	Heater sensor	SWCNT	2.76	1–3	1480–13 350	3270–9800	Neglected
Pop *et al.* (2006)	Self-heating	SWCNT	2.6	1.7	2749	3436	Estimated (6×10^6 K W^{-1})
Li *et al.* (2009)	Raman shift	SWCNT	41	1.8	1810	2400	Measurement independent of boundary resistance
		MWCNT	32	8.2	1400	...	
Pettes and Shi (2009)	Heater sensor	SWCNT	4.31	2.34	>300	>600	Neglected for SWCNTs and DWCNT; estimated for MWCNTs
		SWCNT	2.03	1.5	>580	...	
		DWCNT	4.02	2.7	>540	...	
		MWCNT	1.97	11.4	160	...	
		MWCNT	3.31	14	34	...	
			3.7	9.8	2950	...	
Fujii *et al.* (2005)	T-type sensor	MWCNT	1.89	16.1	1650	...	Neglected
			3.6	28.2	500	...	
Kim *et al.* (2001)	Heater sensor	MWCNT	2.5	14	3000	...	Neglected
Wang, Tang, Zheng *et al.* (2007); Wang, Tang, Li *et al.* (2007)	4-pad 3ω	SWCNT	0.509	1.9	2630	3680	Measurement independent of boundary resistance
			4.919	1.9	3160	4680	
			6.941	1.9	3210	4740	
Choi *et al.* (2005)	2-pad 3ω	MWCNT	1	46		650	Neglected contact resistance
			1.1	42		830	
Choi *et al.* (2006)	4-pad 3ω	MWCNT	1.4	20		300	Measurement independent of boundary resistance

[a] k values using $A = \pi d^2/4$.
[b] k' values using $A = \pi d\delta$, where $\delta = 0.34$ nm.

During electrical self-heating, particularly at high bias, Joule heating generates nonequilibrium in the phonon population (Lazzeri *et al.*, 2005; Pop *et al.*, 2005, 2007; Bushmaker *et al.*, 2007; Oron-Carl and Krupke, 2008; Deshpande *et al.*, 2009). For suspended nanotubes, Joule heating increases the population of optical phonon modes significantly above that of acoustic phonon modes, an effect which has been modeled using distinct temperatures for the two branches (Lazzeri *et al.*, 2005; Pop *et al.*, 2005, 2007; Bushmaker *et al.*, 2007; Oron-Carl and Krupke, 2008; Deshpande *et al.*, 2009). In contrast to the data for suspended nanotubes, the on-substrate nanotube data of Pop *et al.* (2007) could be explained without considering nonequilibrium effects, likely because of shorter optical phonon lifetimes for on-substrate nanotubes. Lazzeri *et al.* (2005) showed that the small electron transport scattering length could be explained by hot optical phonons. Nonequilibrium phonon populations in electrically heated SWCNTs have been detected directly through Raman scattering experiments (Bushmaker *et al.*, 2007; Oron-Carl and Krupke, 2008; Deshpande *et al.*, 2009).

For on-substrate measurements, the thermal contact resistance between the nanotube and the substrate impacts the temperature profile in the nanotube and is critical to determining the intrinsic thermal conductivity. For their measurements using the 3ω method, Wang, Tang, Zheng *et al.* (2007) and Wang, Tang, Li *et al.* (2007) estimated 30%–40% of the total heat power generated in their nanotubes conducted to the substrate. Interaction between the nanotube and the substrate may also directly impact the nanotube thermal conductivity. Measurements of supported graphene (Cai *et al.*, 2010; Seol *et al.*, 2010) show reduced thermal conductivity compared to suspended sheets, suggesting a suppression of some phonon modes. Thermal conduction measurements of carbon nanotube composites (Gojny *et al.*, 2006) suggested that phonon modes and boundary scattering within a nanotube may also be impacted by contacting materials.

Measurement techniques which can extract the intrinsic thermal conductivity separately from the boundary resistance with a substrate require the nanotube to be suspended. While suspended devices for these experiments require more challenging fabrication, confidence in the thermal conductivity measurement is increased and the measured values from different experiments can be directly compared without considering substrate effect. However, even in suspended structures, contact resistances at the ends of the nanotube still need to be considered. In the diffusive regime, it is commonplace to convert the thermal conductance to thermal conductivity by means of $k = G/LA$, which requires important assumptions about the relative importance of contact resistances, as well as the cross-sectional area (as discussed in Sec. II.A). Specifically, when a CNT is suspended between a heater and heat sink, the temperature rise measured between

the heater and heat sink is composed of three parts: (1) the temperature rise due to the contact resistance between the heater and the CNT, (2) the temperature rise due to heat conduction within the CNT, and (3) the temperature rise due to the contact resistance between the CNT and the heat sink. The CNT thermal conductivity can be calculated from the measured temperature drop considering the boundary resistance using

$$k = \frac{L}{A(\Delta T_{\mathrm{CNT}}/\dot{q})} \tag{1a}$$

$$= L/\left\{A\left[\frac{\Delta T_{\mathrm{total}} - \Delta T_{\mathrm{heater\text{-}CNT}} - \Delta T_{\mathrm{CNT\text{-}sink}}}{\dot{q}}\right]\right\} \tag{1b}$$

$$= L/\left\{A\left[\frac{\Delta T_{\mathrm{total}}}{\dot{q}} - R_{\mathrm{heater\text{-}CNT}} - R_{\mathrm{CNT\text{-}sink}}\right]\right\}. \tag{1c}$$

The use of Eq. (1c) yields a higher thermal conductivity than when the thermal boundary resistance is neglected Eq. (1a). Decreasing the thermal contact resistance, such as by increasing the area of contact or reducing the intrinsic interface resistance, reduces the portion of the total thermal resistance due to contacts and provides a more accurate thermal conductivity value. For ballistic transport along a nanotube, the thermal conductance depends on the transmissivity of the contacts and is independent of the nanotube length. When extracting thermal conductivity from ballistic conductance data, the result incorporates contact effects. More details on ballistic and diffusive transport are presented in Secs. II.D.1.a and II.D.2.

Many working with suspended devices have attempted to account for or estimate the impact of the contact resistance at the ends of the nanotubes in measurements of the thermal conductance. Kim *et al.* (2001) estimated a thermal contact conductance of 5×10^{-7} W K^{-1} for a 14 nm diameter MWCNT suspended over a trench with 1 μm of the overlap between the CNT and the resistive elements as shown in the left panel of Fig. 1. When compared to the total nanotube conductance of 1.6×10^{-7} W K^{-1}, about 68% of the total resistance of the nanotube is due to the intrinsic thermal resistance of the nanotube compared to the contact resistance. This suggests the true thermal conductivity is about 1.5 times the reported value. Pettes and Shi (2009) found that depositing Pt-C at the MWCNT-membrane contacts significantly reduced the total thermal resistance of the nanotube including both volume and contact components compared to the as-grown case. For the three MWCNT samples measured, the contact resistance after Pt-C deposition was estimated to be 12%–54% of the total resistance allowing the intrinsic thermal conductivity to be estimated. To account for the contact resistance between the nanotube and substrate in the self-heating measurement of suspended SWCNTs, Pop *et al.* (2006) used the fact that typical interfaces between dense materials have thermal interface resistance in the range of $(1\text{–}3) \times 10^{-8}$ m^2 K W^{-1} (Cahill *et al.*, 2003). The contact area was approximated as the product of the nanotube diameter and the length of overlap between the substrate and the nanotube, using $A_c = dL_C$ where $L_C \sim 2$ μm and $d \sim 1.7$ nm. This resulted in a total thermal contact resistance between 3×10^6 and 9×10^6 K W^{-1} and yielded about 10% uncertainty in the extracted thermal conductivity. In an early work by Choi *et al.* (2005), using a two-point 3ω technique, the contact resistance was deemed negligible when the measurements of total thermal resistance of several MWCNTs of different lengths and diameters followed the expected relationship for the intrinsic resistance. Raman spectroscopy can be used to measure the temperature profile along the axis of the CNT based on the shift in the G band Raman frequency (Hsu *et al.*, 2008). The relative magnitude thermal boundary resistance and intrinsic thermal resistance of a nanotube can be compared by combining (laser or electrical) heating of suspended nanotubes with Raman thermometry. Hsu *et al.* (2008) found that the boundary resistance ranged from 0.02 to 17 times the intrinsic thermal resistance of the CNT depending on the quality of the nanotube and the contact. For additional discussion of the CNT-substrate boundary resistance, see Sec. III.D.

C. Theoretical progress

There are detailed theoretical studies of carbon nanotube thermal transport that complement the experimental data in the previous section. Transport of thermal energy in carbon nanotubes is primarily through atomic vibrations. Carbon nanotubes have a high aspect ratio with diameters on the order of nanometers and lengths as long as millimeters and can span the range from ballistic conductors to diffusive conductors. As mentioned in Sec. II.A, carbon nanotubes are ballistic conductors when the mean free path is longer than the nanotube length and the dominant phonon wavelength is smaller than the nanotube diameter. Diffusive heat transport dominates when the CNT is much longer than both the phonon mean free path and the dominant phonon wavelength and the energy carriers scatter many times within the nanotube.

Ballistic transport can be modeled with a Landauer approach (see Sec. II.C.1) and modifications to the ballistic transport models have been proposed to extend the estimation of the thermal properties into the diffusive regime (Wang and Wang, 2006; Shang, Ming, and Wang, 2007). Strong mesoscopic effects modify the heat transfer characteristics in an intermediate regime, where the nanotube is much longer than the phonon mean free path and the dominant phonon wavelength is larger than the diameter of the nanotube, but shorter than the nanotube length (Prasher, Tong, and Majumdar, 2007). In the same nanotube, ballistic or mesoscopic conduction is often observed at low temperatures, while diffusive conduction exists at higher temperatures.

Phonon transport models (Sec. II.C.2) and molecular dynamics simulations (Sec. II.C.3) have also been used to investigate heat transport in carbon nanotubes. Phonon transport theory calculates the evolution of phonon populations in carbon nanotubes using, for example, the Boltzmann transport equation. Key parameters for these models include the phonon dispersion relationships and the scattering or relaxation times for different phonon interactions, which must be determined from experiments or treated as inputs from more fundamental models. Molecular dynamics simulations allow for calculation of thermal properties based on the dynamics of the atoms interacting through interatomic potentials. Several different proposed forms for the interaction potential between the atoms have been investigated.

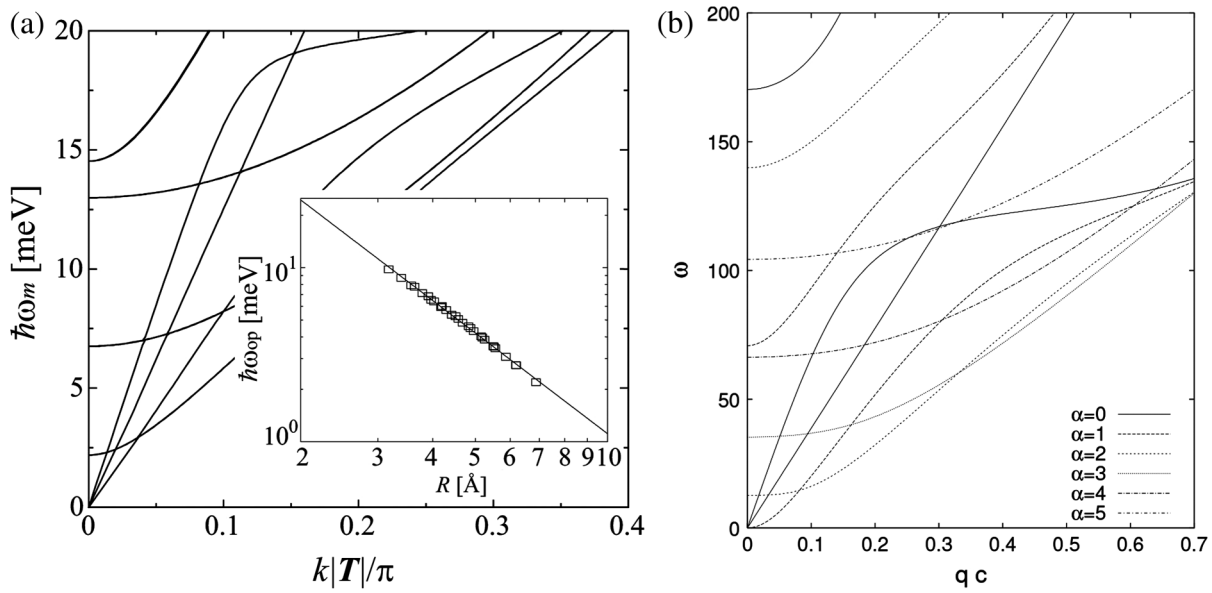

FIG. 2. (a) Phonon dispersion relationship for (10,10) nanotube calculated by Yamamoto, Watanabe, and Watanabe (2004b). The inset shows that the energy gap of the lowest optical mode ($\hbar\omega_{op}$) decreases with nanotube radius. With this model, all four acoustic modes exhibit a linear dispersion relationship because the impact of bond bending is neglected. (b) Phonon dispersion relationship for (10,10) armchair nanotube calculated by Mahan and Jeon (2004). Two transverse (''flexure'') modes exhibit a quadratic dispersion relationship, while the longitudinal and twist modes are linear.

1. Landauer approach

The long mean free paths of phonons in carbon nanotubes compared to those in other materials cause the nanotube to exhibit strong ballistic behavior over submicron length scales. Ballistic quantized thermal conductance in quantum wires was investigated by Rego and Kirczenow (1998). Ballistic thermal conductance for one-dimensional conductors results in the quantum of thermal conductance, which can be derived using Landauer theory. For a one-dimensional system between a hot and cold heat bath, assuming perfect transmission at the interfaces, adiabatic system-heat bath contacts, and a linear temperature response regime (Yamamoto, Watanabe, and Watanabe, 2004a, 2004b), the phonon thermal conductance in the limit where $\Delta T \ll T$ is

$$G_{\text{phonon}} = \frac{\dot{q}_{\text{phonon}}}{\Delta T} = \frac{k_B^2 T}{2\pi\hbar} \int_{x_m^{\min}}^{x_m^{\max}} \frac{x^2 e^x}{(e^x - 1)^2} dx, \tag{2}$$

where

$$x = \frac{\hbar\omega}{k_B T}, \qquad T = \frac{T_{\text{hot}} + T_{\text{cold}}}{2},$$

and m denotes the phonon branches. Each gapless acoustic phonon mode, independent of the exact dispersion relation, contributes a quantum of thermal conductance

$$G_{\text{th}} = \frac{\pi^2 k_B^2}{3h} T. \tag{3}$$

For temperatures below the optical subband excitation temperature, the four modes contribute to the heat transport in quantum wires (Rego and Kirczenow, 1998) and single-wall nanotubes (Yamamoto, Watanabe, and Watanabe, 2004a, 2004b). Calculations of the dispersion relationship for various chiralities of single-wall cabon nanotubes have shown four phonon modes at low temperature (Mahan and Jeon, 2004; Yamamoto, Watanabe, and Watanabe, 2004a, 2004b; Mingo and Broido, 2005a), which yields $G = 4G_{\text{th}}(T)$ in the low temperature limit. Figure 2 shows two examples of the calculated dispersion relationship for a (10,10) single-wall carbon nanotube. In early work, using zone-folding models (Jishi *et al.*, 1993; Saito, Dresselhaus, and Dresselhaus, 1998; Saito, Takeya *et al.*, 1998; Yamamoto, Watanabe, and Watanabe, 2004a, 2004b), all four of the four acoustic modes had linear dispersion relationships [see, e.g., Yamamoto, Watanabe, and Watanabe (2004b)], as shown in Fig. 2(a). Mahan and Jeon (2004) showed that for CNTs, as the bonds are bent relative to the straight bonds in graphite or a graphene sheet, both the magnitude and symmetry rules used in the force-constant models must be modified. They showed that the previously derived (Jishi *et al.*, 1993; Saito, Dresselhaus, and Dresselhaus, 1998; Saito, Takeya *et al.*, 1998; Yamamoto, Watanabe, and Watanabe, 2004a, 2004b) linear dispersion relationship of the transverse modes should in fact be a quadratic relationship as shown in Fig. 2(b). Quadratic dispersion relations for the transverse modes were obtained by using several molecular dynamics models (Popov, Van Doren, and Balkanski, 2000; Popov, 2002, 2004; Mahan and Jeon, 2004), as well as *ab initio* calculations (Sánchez-Portal *et al.*, 1999), and it is now widely accepted that the doubly degenerate transverse modes should have a quadratic dependence. The energy gap of the lowest optical mode ($\hbar\omega_{op}$) depends on the radius of (n, n) single-wall carbon nanotubes as $\hbar\omega_{op} \sim R^{-2}$ [see the inset of Fig. 2(a)].

Optical phonon modes begin to contribute to heat transfer as temperature increases above a few degrees Kelvin depending on the energy of the lowest optical phonon mode, which depends on the diameter of the nanotube (Yamamoto, Watanabe, and Watanabe, 2004a). Extending the estimate of the thermal conductance of SWCNTs in the low temperature limit ($G = 4G_{\text{th}}$) to higher temperatures is possible by considering the chirality of the nanotube in determining the

number of phonon modes for thermal conductance (Saito, Dresselhaus, and Dresselhaus, 1998; Brown *et al.*, 2005; Shang, Ming, and Wang, 2007). The number of phonon modes for a single-wall carbon nanotube (or in a single shell of a multiwall carbon nanotube) in the ballistic regime is determined by the chirality (Saito, Dresselhaus, and Dresselhaus, 1998; Brown *et al.*, 2005; Shang, Ming, and Wang, 2007)

$$N_{\mathrm{ph}} = \frac{12(n^2 + mn + m^2)}{d_R} = \frac{12\pi^2 d_j^2}{a_o^2 d_R}, \tag{4}$$

where (n, m) is the chiral vector, d_R is the greatest common divisor of $(2n + m)$ and $(2m + n)$, d_j is the diameter of the nanotube, and $a_o = \sqrt{3}b_o$ is the length of the unit chiral vector, where $b_o = 0.142$ nm is the equilibrium interatomic distance. The nanotube diameter can also be calculated from the chiral vector:

$$d_j = \frac{a_o}{\pi}\sqrt{n^2 + mn + m^2}. \tag{5}$$

Each phonon mode can transport a quantum of thermal conductance in the ballistic regime. Thus the total ballistic thermal conductance of a single-wall carbon nanotube or one shell in a multiwall carbon nanotube is $G_j = N_{\mathrm{ph}} G_{\mathrm{th}}$. For a multiwall carbon nanotube, the total ballistic thermal conductance is the sum of the conductance of each shell (Shang, Ming, and Wang, 2007), $G = \sum_{N_{\mathrm{shells}}} G_j$. This treatment neglects coupling between shells. Brown *et al.* (2005) measured the thermal conductance of MWCNTs to be consistent with this method within the range of the expected number of phonon channels (100s to 1000). The conductance calculation can be extended to a bundle of nanotubes of mixed diameters by summation of the conductance of the individual nanotubes (Shang, Ming, and Wang, 2007).

To extend the ballistic model of thermal conductance into the diffusive regime, Shang, Ming, and Wang (2007) extended previous modeling work (Che, Cagin, and Goddard, III, 2000; Chantrenne and Barrat, 2004; Mingo and Broido, 2005b) showing that thermal conductivity of carbon nanotubes stops increasing at lengths longer than the mean free path of the phonons, indicative of diffusive conduction. This suggests that for nanotube lengths greater than the phonon mean free path l, the thermal conductance should vary according to

$$G_{j,\mathrm{diffuse}} = G_{j,\mathrm{ballistic}} \frac{l}{L}. \tag{6}$$

In other words, the total thermal conductance for nanotubes of any length can be expressed as

$$G_j = \begin{cases} N_{\mathrm{ph}} G_{\mathrm{th}} & \text{for } L < l, \\ N_{\mathrm{ph}} G_{\mathrm{th}} l/L & \text{for } L > l. \end{cases} \tag{7}$$

In the derivation of the ballistic quantum conductance, perfect transmission was assumed at both heat baths. Wang and Wang (2006) modified the energy transmission ζ for the ballistic to diffusive transition regime, where the mean free path is on the order of the CNT length, using $\zeta = l/(l + L)$, and in the diffusive regime $(L > l)$, using $\zeta = l/L$. This provides a smooth crossover between the ballistic and the diffusive regimes. Similarly, Yamamoto *et al.* (2009) derived an expression for the thermal conductance valid from the ballistic to the diffusive regime given by

$$G = \sum_m \int_{\omega_m^{\min}}^{\omega_m^{\max}} \frac{d\omega}{2\pi}\left[\frac{df(\omega, T)}{dT}\right]\frac{l_m(\omega)}{L + l_m(\omega)}, \tag{8}$$

where T is an average temperature, $\hbar\omega_m$ is the phonon energy, $f(\omega, T)$ is the distribution of phonons, and $l_m(\omega)$ is the mean free path of phonons in the mth phonon mode. Equation (8) reduces to the ballistic thermal conductance for CNTs with lengths much shorter than the mean free path and to the Peierls-Boltzmann equation for CNTs of much longer lengths (Yamamoto *et al.*, 2009). Estimating the mean free path using an expression for three-phonon umklapp processes where $\hbar\omega/k_B T \gg 1$ yields

$$l_m(\omega) = \frac{c_m A}{\omega^2 T}, \tag{9}$$

where A is the coupling constant (using the value for graphene, $A = 3.35 \times 10^{23}\ \mathrm{m\,K\,s^{-2}}$) and c_m is a parameter used to represent the curvature of the CNT, allows the thermal conductance to be calculated from

$$G = \frac{k_B}{2\pi}\sum_m \Omega_m\left[\arctan\left(\frac{\omega_m^{\max}}{\Omega_m}\right) - \arctan\left(\frac{\omega_m^{\min}}{\Omega_m}\right)\right], \tag{10}$$

where $\Omega_m = \sqrt{c_m A/TL}$, which can be considered a length-dependent characteristic frequency. The thermal boundary resistance can be included by adding the inverses of the conductances $G_{\mathrm{total}}^{-1} = G^{-1} + G_{\mathrm{int}}^{-1}$. Using a curvature parameter value of $c_m = 0.65$ and a thermal boundary resistance of $G_{\mathrm{int}}^{-1} = 0.09\ \mathrm{K\,nW^{-1}}$, the analytical model matches well with molecular dynamic simulations of a (3,3) nanotube (Yamamoto *et al.*, 2009).

2. Phonon transport calculations

Predictions of nanotube thermal conductivity stem from descriptions of the wave vector models describing the transport of phonons within a CNT. Wave vector models begin from kinetic theory and require knowledge of the specific heat, the phonon group velocity, the mean free path, or relaxation time. Solutions to the Peierls-Boltzmann equation, which describes the transport of phonons within a material, allow calculation of the thermal conductivity without making the relaxation time approximation.

Chantrenne and Barrat (2004) developed an analytical model of thermal conductivity by analysis of the phonon spectrum with properties dependent on the wave vector. The thermal conductivity in the x direction k_x becomes

$$k_x = \sum_q \sum_m C_m(q)\upsilon_m^2(q)\tau_m(q)\cos^2(\Theta_m(q)), \tag{11}$$

where $C_m(q)$ and $\upsilon_m(q)$ are the specific heat and group velocity of the phonon with wave vector q, and polarization (branch index) m, $\tau_m(q)$ is the phonon relaxation time due to scattering for the mode, and $\Theta_m(q)$ is the angle between the wave vector q and the direction x. Cao *et al.* (2004), Yan, Xiao, and Li (2006), and Wang, Tang, Zheng *et al.* (2007) formulate comparable models, but neglect the cosine term. Through the dispersion curve, the dependence on the wave vector q can be transformed into the angular frequency ω. The scattering mechanisms include three-phonon (umklapp) processes, boundary scattering, and defect scattering and the total relaxation time can be computed through

$$\tau^{-1}(\omega) = \tau_u^{-1}(\omega) + \tau_{\mathrm{BC}}^{-1}(\omega) + \sum_{i=1}^{N_d} \tau_{D,i}^{-1}(\omega), \tag{12}$$

where τ_u is the relaxation time due to umklapp processes, τ_{BC} is the relaxation time due to boundary scattering, $\tau_{D,i}$ is the relaxation time due to the ith defect, and N_d is the total number of defects (including impurities, isotopes, vacancies, etc.). To validate their wave vector model, Chantrenne and Barrat (2004) calculated the thermal conductivity of a cube of argon and compared the predictions with results from nonequilibrium molecular dynamics (NEMD) simulations of the same system. Upon finding good agreement between the models, the wave vector model was extended to sheets of graphene and carbon nanotubes.

Approximations for the relaxation times must be used to estimate thermal conductivity and several forms are plausible for the relaxation time due to umklapp processes. Chantrenne and Barrat (2004) expressed the temperature and frequency dependence of the umklapp relaxation time as

$$\tau_u^{-1}(\omega) = A\omega^2 T^{\xi} \exp\left(-\frac{B}{T}\right), \tag{13}$$

where A, B, and ξ are fitted to the temperature variations of the bulk thermal conductivity, although in their calculations they used a simplified expression $\tau_u^{-1}(\omega) = A_1(T)\omega^2$, where A_1 is determined by fitting the calculated thermal conductivity to the measured bulk thermal conductivity of the material. Since the bulk thermal conductivity of the carbon nanotubes is unknown, an arbitrary value of A_1 was chosen and the variations in thermal conductivity were calculated rather than the absolute magnitude.

Both Cao *et al.* (2004) and Yan, Xiao, and Li (2006) defined the first-order relaxation time for umklapp scattering as

$$\tau_u^{-1}(q) = \frac{4\gamma^2 h}{3} \sum_{q'} \frac{F(\omega, v, N_0)}{\rho}, \tag{14}$$

where

$$F(\omega, v, N_0) = \left[\frac{\omega\omega'\omega''(N_0' - N_0'')}{v_g^2}\right]\delta(\omega + \omega' - \omega''), \tag{15}$$

ρ is the mass density, and N_0' and N_0'' are the equilibrium occupancies of q' and q'' phonons. Wang, Tang, Zheng *et al.* (2007) considered the first-order three-phonon umklapp process with a relaxation time of

$$\tau_{1,u}^{-1}(\omega) = A\omega^2 \frac{T}{T_0}, \tag{16}$$

but also included the umklapp scattering to second order:

$$\tau_{2,u}^{-1}(\omega) = \frac{32}{27}\gamma^4 \left(\frac{T}{T_0}\right)^2 \omega_b, \tag{17}$$

where $A = 4\pi a\gamma^2/v$, T_0 is the characteristic temperature of the material, $T_0 = Mv^2/k_B$, a^3 is the atom volume, M is the atom mass, γ is the Grüneisen parameter, and ω_b is the phonon branch frequency at the zone boundary. Additionally, Wang, Tang, Zheng *et al.* (2007) considered N-phonon processes in the calculation of the total relaxation time τ.

Boundary scattering should also be included in a comprehensive thermal conductivity model. The relaxation time due to the boundary scattering is given by

$$\tau_{\mathrm{BC}}^{-1} = v(q, m)\frac{1 - s}{L(q)}, \tag{18}$$

where s is the fraction of all phonons which scatter specularly from the boundaries ($s \in [0 - 1]$) and $L(q)$ is the distance a phonon with wave vector q and polarization m can travel between boundary surfaces (Chantrenne and Barrat, 2004; Wang, Tang, Zheng *et al.*, 2007). In contrast, some set the relaxation time for the boundary scattering to 50 ps (Hone *et al.*, 1999; Cao *et al.*, 2004; Yan, Xiao, and Li, 2006), independent of temperature and phonon energy, an approach that is supported by experimental and theoretical work (Casimir, 1938; Rego and Kirczenow, 1998; Hone *et al.*, 1999; Hone, Batlogg *et al.*, 2000; Kim *et al.*, 2001). Experimental measurements (Hone *et al.*, 1999) of the thermal conductivity of a nanotube rope at low temperatures (< 30 K) suggest an energy-independent mean free path consistent with boundary scattering. Similarly Kim *et al.* (2001) observed a temperature-independent component of the mean free path on the order of the length of the nanotube. Cao *et al.* (2004) and Yan, Xiao, and Li (2006) investigated the effect of different chiralities in SWCNTs using wave vector models. Yan, Xiao, and Li (2006) extended the model to multiwall nanotubes and investigated the differences between strong and weak coupling between walls in multiwall nanotubes. Table II summarizes different phonon transport models highlighting the different models for umklapp and boundary scattering relaxation times.

The transport of phonons in a solid can be calculated using the Peierls-Boltzmann phonon transport equation (Mingo and Broido, 2005b):

TABLE II. Phonon transport model summary.

Reference	Chiralities	Umklapp scattering	Boundary scattering	Comments
Chantrenne and Barrat (2004)	(9,0) (18,0) (36,0)	$\tau_u^{-1}(\omega) = A_1(T)\omega^2$	$\tau_{\mathrm{BC}}^{-1} = v(q, m)\frac{1-s}{L(q)}$	System size varied
Wang, Tang, Zheng *et al.* (2007)		$\tau_{1,u}^{-1}(\omega) = A\omega^2\frac{T}{T_0}$, $\tau_{2,u}^{-1}(\omega) = \frac{32}{27}\gamma^4(\frac{T}{T_0})^2\omega_b$	$\tau_{\mathrm{BC}}^{-1} = v(q, m)\frac{1-s}{L(q)}$	N-phonon processes included; length and temperature varied
Yan, Xiao, and Li (2006)	(5,5) to (20,20) (5,0) to (20,0)	$\tau_u^{-1}(q) = \frac{4\gamma^2 h}{3}\sum_{q'}\frac{F(\omega,v,N_0)}{\rho}$	$\tau_{\mathrm{BC}} = 50$ ps	Length and temperature varied; MWCNT; weak and strong coupling
Cao *et al.* (2004)	(6,0) to (14,0)	$\tau_u^{-1}(q) = \frac{4\gamma^2 h}{3}\sum_{q'}\frac{F(\omega,v,N_0)}{\rho}$	$\tau_{\mathrm{BC}} = 50$ ps	Temperature varied

$$-v_P \frac{dn_p}{dx} = \left(\frac{\partial n_p}{\partial t}\right)_C, \tag{19}$$

where $p = \{q, m\}$ is the phonon wave vector q and the branch index m, n_p is the distribution function, v_p is the phonon group velocity, and $(\partial n_p/\partial t)_C$ is from the collision of phonons. Mingo and Broido (2005b) iteratively solved the Peierls-Boltzmann phonon transport equation for single-wall carbon nanotubes with a linearized form of the collision term $(\partial n_p/\partial t)_C$ and scattering due to three-phonon processes (up to second order). When only first-order three-phonon processes are included, the thermal conductivity diverges with the nanotube length. Second-order processes must also be included for the thermal conductivity to saturate with length. From the solution to the Peierls-Boltzmann equation, the thermal conductivity can be computed without making the relaxation time approximation. At 316 K, for a (10,0) nanotube, the thermal conductivity saturates to ~4000 $\mathrm{W\,m^{-1}\,K^{-1}}$, but this is only an estimate due to the approximation used for the second-order three-phonon process.

3. Molecular dynamics simulations

Molecular dynamics simulations compute thermal transport based on the interaction potentials between the carbon atoms. Several different empirical forms of the atomic interaction potential have been proposed (Tersoff, 1988a, 1988b, 1989; Brenner, 1990; Yamaguchi and Maruyama, 1998; Stuart, Tutein, and Harrison, 2000; Brenner *et al.*, 2002). Lepri, Livi, and Politi (2003) described in detail molecular dynamics simulations in low-dimensional lattices. Simulations based on equilibrium molecular dynamics (EMD), nonequilibrium molecular dynamics (Osman and Srivastava, 2001; Maruyama, 2002, 2003; Osman and Srivastava, 2005; Zhang and Li, 2005; Zhang, Fan, and Yuen, 2006), and homogeneous nonequilibrium molecular dynamics (HNEMD) (Berber, Kwon, and Tománek, 2000; Zhang *et al.*, 2004) were fruitful even before experiments on individual nanotubes were developed. EMD simulations use the Green-Kubo formula derived from linear response theory (Zhong and Lukes, 2004; Lukes and Zhong, 2007):

$$k_{\alpha\beta} = \frac{1}{Vk_BT^2}\int_0^\infty \langle J_\alpha(t)\cdot J_\beta(t)\rangle dt, \tag{20}$$

where $k_{\alpha\beta}$ is the (α, β) component of the thermal conductivity tensor, V is the volume, and J_α and J_β are the components of the heat current in the α and β directions, respectively. NEMD simulations use the Fourier conduction law to determine the thermal conductivity by applying either a fixed temperature gradient or heat flux to the system. The thermal conductivity is related to the thermal gradient by (Zhong and Lukes, 2004)

$$J_\alpha = -\sum_\beta k_{\alpha\beta}\frac{\partial T}{\partial x_\beta}, \tag{21}$$

where $\partial T/\partial x_\beta$ is the thermal gradient along the β direction. HNEMD simulations apply an external field to mimic the heat flow without actually applying a heat flux or temperature gradient (Zhong and Lukes, 2004).

Table III summarizes the results of many of the different molecular dynamics simulations reported in the literature. As with the experimental results, the MD calculations require definitions of the cross-sectional area for heat transport. For single-wall nanotube simulations, most select the area $A = \pi d\delta$ with δ ranging from 0.1 to 0.34 nm. For comparison, the results of all experimental and modeling reviewed here are standardized using $A = \pi d_o^2/4$, although also shown in Table III are values for k', the thermal conductivity calculated with $A = \pi d\delta$, where $\delta = 0.34$ nm.

Classical molecular dynamics simulations omit the quantum effects that are important for quantitative predictions of the heat capacity and thermal conductivity at temperatures below the Debye temperature (Li, 2000; Sinha and Goodson, 2005). Even at room temperature, these quantum effects must be considered for CNTs as their Debye temperature is much higher than room temperature (Maruyama, 2003; Lukes and Zhong, 2007). Various quantum corrections have been developed to improve the predictions of the MD simulations below the Debye temperature (Che, Cagin, and Goddard, III, 2000; Lukes and Zhong, 2007; Wu and Hsu, 2009); however, the applicability of these corrections is still subject to debate (Turney, McGaughey, and Amon, 2009). Nevertheless, thermal conduction in CNTs is dominated by low frequency (long wavelength) phonons which exhibit nearly classical behavior at room temperature (Grujicic, Cao, and Gersten, 2004; Grujicic, Cao, and Roy, 2005). Therefore, both classical and quantum corrected MD simulations should still provide useful qualitative trends in thermal conductivity (such as with diameter or length) and arguably acceptable values of thermal conductivity.

Many reports have simulated thermal conduction of CNTs with a chiral vector of (10,10) yielding values from 80 $\mathrm{W\,m^{-1}\,K^{-1}}$ (Zhong and Lukes, 2004) to 6600 $\mathrm{W\,m^{-1}\,K^{-1}}$ (Berber, Kwon, and Tománek, 2000) at 300 K, with one extreme outlier at 10^{23} $\mathrm{W\,m^{-1}\,K^{-1}}$ (Yao *et al.*, 2005). Variations in the nanotube length, boundary conditions, molecular dynamics methods (EMD, NEMD, and HNEMD), and interatomic potentials contribute to the range of simulated values. The results for (10,10) carbon nanotubes simulated using Brenner-type potential at lengths of 30 to 40 nm highlight the range of variation when using different MD methods. Specifically, the extracted thermal conductivity values include 300 $\mathrm{W\,m^{-1}\,K^{-1}}$ from EMD simulations (Maruyama, 2003), 880 $\mathrm{W\,m^{-1}\,K^{-1}}$ from NEMD simulations (Che, Cagin, and Goddard, III, 2000), and 2200 $\mathrm{W\,m^{-1}\,K^{-1}}$ from HNEMD simulations (Zhang *et al.*, 2004). Results from several NEMD simulations of (10,10) with nanotube lengths on the order of 20 to 200 nm range from 355 to 1700 $\mathrm{W\,m^{-1}\,K^{-1}}$ (Osman and Srivastava, 2001; Maruyama, 2002, 2003; Padgett and Brenner, 2004; Zhang and Li, 2005) using a range of interatomic potentials based on the Tersoff (1989) and Brenner (1990) potentials. With the exception of the results from Osman and Srivistava of 1700 $\mathrm{W\,m^{-1}\,K^{-1}}$, the remaining results for Tersoff- and Brenner-type potentials range from 355 to 560 $\mathrm{W\,m^{-1}\,K^{-1}}$. Similarly, results using the *ab initio* force field COMPASS (condensed-phase optimized molecular potentials for atomistic simulation studies) yielded 300 $\mathrm{W\,m^{-1}\,K^{-1}}$ (Zhang,

TABLE III. Molecular dynamics simulations summary. Room temperature thermal conductivity values for the maximum length simulated. REBO: reactive empirical bond order; AIREBO: adaptive intermolecular reactive empirical bond order.

Reference	Chirality	L (nm)	D (nm)	k[a] ($\mathrm{W\,m^{-1}\,K^{-1}}$)	k'[b] ($\mathrm{W\,m^{-1}\,K^{-1}}$)	Sim. type	Potential	Converged with length?
Che, Cagin, and Goddard, III (2000)	(10,10)	<40	1.36	880	880	EMD	Brenner (1990)	Yes (> 10 nm)
Padgett and Brenner (2004)	(10,10)	<1500	1.351	355	350	NEMD	2nd generation REBO (Brenner *et al.*, 2002)	Yes (> 150 nm)
Grujicic, Cao, and Gersten (2004); Grujicic, Cao, and Roy (2005)	(10,10) (18,0) (14,6)	2.477–39.632 2.145–34.320 3.813–30.504	1.351 1.404 1.387	895 790 765	890 815 780	EMD	AIREBO (Stuart, Tutein, and Harrison, 2000)	Yes ($\gtrsim$ 10 nm)
Osman and Srivastava (2001)	(5,5) (10,10) (15,5) (10,0)	Aspect ratio of 10–20 (~22 nm)	0.68 1.36 1.41 0.78	4500 1700 1640 3900	2250 1700 1700 2250	NEMD	Tersoff-Brenner (Tersoff, 1988a; Brenner, 1990)	Not investigated; periodic boundary conditions; assumed to be long enough because of the results of Che, Cagin, and Goddard, III (2000)
Zhang, Fan, and Yuen (2006)	(5,5) (6,6) (8,8) (10,10)	12.2 and 24.4	0.68 0.81 1.08 1.35	410 435 365 300	205 260 290 300	NEMD	COMPASS	Variation between 12.2 and 24.4 nm results
Zhang and Li (2005)	(9,0) (10,0) (5,5)	0.1–100	0.714 0.794 0.686	710 560 810	370 330 410	NEMD	Tersoff (1989)	No
Maruyama (2002)	(5,5) (10,10)	6–404	0.68 1.36	1000 400	500 400	NEMD	Tersoff-Brenner (Brenner, 1990)	No
Maruyama (2003)	(5,5) (8,8) (10,10)	12–404	0.68 1.09 1.36	1350 560 400	675 450 400	NEMD	Simplified Brenner (Brenner, 1990; Yamaguchi and Maruyama, 1998)	No
Yao *et al.* (2005)	(5,5) (10,10) (15,15)	6–100	0.68 1.36 2.03	$\sim 10^{24}$ $\sim 10^{23}$ $\sim 10^{22}$	$\sim 10^{23}$ $\sim 10^{23}$ $\sim 10^{22}$	EMD	Tersoff (1989)	No
Lukes and Zhong (2007)	(10,1)	5–40 5–10	1.36	120–150[c] 240–375[c]	120–150[c] 240–375[c]	EMD HNEMD	2nd generation REBO (Brenner *et al.*, 2002) and Lennard-Jones	No (free and periodic BC tested) No
Berber, Kwon, and Tománek (2000)	(10,10)	2.47	1.36	6600	66 000	HNEMD	Tersoff (1988b)	Not investigated (periodic boundary conditions)
Qiu *et al.* (2012)	(5,5)–(21,21) (9,0)–(36,0)	50–400	0.7–2.9	2000–900[d]	1000–2000[d]	NEMD	Optimized Tersoff (Lindsay and Broido, 2010)	No. Extrapolated to bulk limit ($L \to \infty$) by fitting $1/k - 1/L$ relation
Zhang *et al.* (2004)	(10,10) (11,11) (10,13) (20,0)	... 30 29 26	1.36 1.49 1.56 1.57	2200 3190 870 6730	2200 3500 1000 7750	HNEMD	Brenner (1990)	Not investigated (periodic boundary conditions)

[a] k values using $A = \pi d^2/4$.
[b] k' values using $A = \pi d\delta$, where $\delta = 0.34$ nm.
[c] Variations due to fitting method.
[d] Variations due chirality and diameter. Range shown with increasing D.

Fan, and Yuen, 2006) for short (10,10) nanotubes. Qiu *et al.* (2012) extrapolated their results simulated for short nanotube lengths to infinitely long nanotubes finding thermal conductivities of 700 and 1650 $\mathrm{W\,m^{-1}\,K^{-1}}$ using the Tersoff potential (Tersoff, 1988a) and an optimized version of the Tersoff potential, which better modeled anharmonicity and phonon dispersion (Lindsay and Broido, 2010), respectively. The effect of nanotube length is discussed in detail later in this review in combination with experimental data. Some of the MD work discussed here did not consider the effect of length in the simulations. Thus, it is unclear whether those MD results can be compared to the experiments with the long CNTs.

Molecular dynamics simulations have also been developed to probe inter-CNT contact resistance and the resistance between a substrate and a CNT. More details on these simulations can be found in Sects. III.B and III.D, respectively.

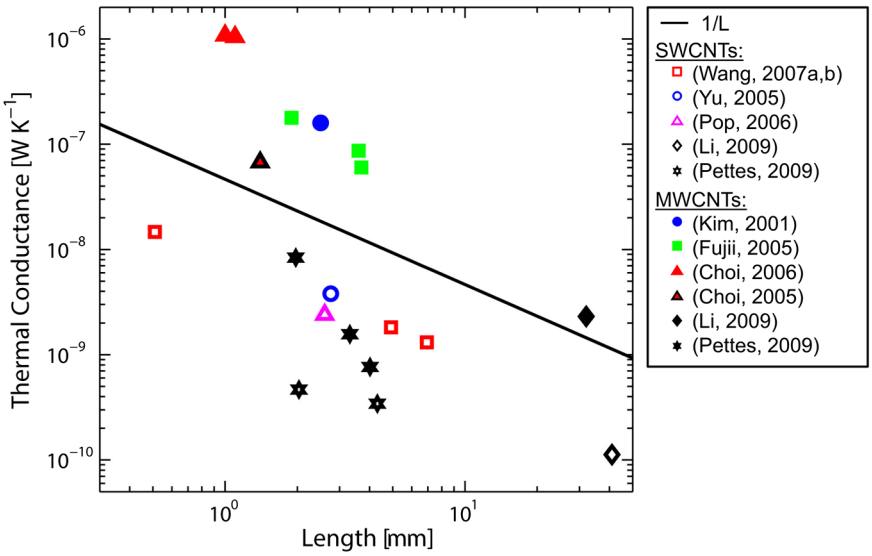

FIG. 3 (color online). Room temperature thermal conductance of carbon nanotubes as a function of length. The solid line indicates the $1/L$ trend expected for a fixed thermal conductivity, i.e., diffusive conduction in nanotubes. Solid symbols denote MWCNTs, while open symbols denote SWCNTs.

D. Summary of key findings

1. Geometrical effects

a. Length

Thermal conduction transitions from the ballistic to the diffusive conduction regime as the nanotube length increases. The phonon mean free path depends on temperature such that for the same nanotube ballistic conduction can be observed at low temperature, while diffusive conduction prevails at room temperature. In the ballistic conduction regime, the thermal conductance $G_{\text{ballistic}}$ is fixed and the thermal conductivity apparently increases with nanotube length as $k = G_{\text{ballistic}}L/A$. The thermal conductivity reaches a constant value at lengths much longer than the mean free path, where the conduction is diffusive. Figure 3 shows experimental data for the thermal conductance of single-wall (Yu *et al.*, 2005; Pop *et al.*, 2006; Wang, Tang, Zheng *et al.*, 2007; Wang, Tang, Li *et al.*, 2007; Li *et al.*, 2009; Pettes and Shi, 2009) and multiwall (Kim *et al.*, 2001; Choi *et al.*, 2005; 2006; Fujii *et al.*, 2005; Li *et al.*, 2009; Pettes and Shi, 2009) nanotubes at room temperature. The majority of the available experimental data is for nanotubes longer than 0.5 μm. Since the conductance data of the nanotubes follow approximate inverse proportionality with length, it appears that these nanotubes behave diffusively and have lengths much longer than the mean free path. Despite the varying diameters, and perhaps also varying chiralities, of the various nanotubes characterized, the $1/L$ trend remains present. Figure 4 compares experimentally measured thermal conductances (Yu *et al.*, 2005; Pop *et al.*, 2006; Wang, Tang, Zheng *et al.*, 2007; Wang, Tang, Li *et al.*, 2007; Li *et al.*, 2009) with the predictions of several modeling efforts (Pop *et al.*, 2006; Wang and Wang, 2006; Shang, Ming, and Wang, 2007; Wang, Tang, Zheng *et al.*, 2007) for SWCNTs of approximately the same diameters (1.4 to 1.9 nm). The ballistic conductance model (Shang, Ming, and Wang, 2007), with the extension to the diffusive regime as discussed in Sec. II.C.1, was plotted for two chiralities of nanotubes with diameters of approximately 1.9 nm: a (24,0) zigzag nanotube with a 1.88 nm diameter and a (14,14) armchair nanotube with a 1.89 nm diameter. Although not included in the figure, the predictions of the model of Yamamoto *et al.* (2009) yield a smooth transition from the ballistic to the diffusive regime by considering the length dependence of the umklapp scattering processes [Eq. (9)] and compare well with molecular dynamics simulations of the (3,3) and (5,5) SWCNTs. An empirical model (Pop *et al.*, 2006), developed from an analytical fit to the temperature dependency of the measured thermal conductivity for a 1.7 nm SWCNT in conjunction with additional data from (Yu *et al.*, 2005), predicts a thermal conductivity given by

$$k' = \left[3.7 \times 10^{-7}\ T + 9.7 \times 10^{-10}\ T^2 + 9.3\left(1 + \frac{0.5}{L}\right) T^{-2}\right]^{-1}, \tag{22}$$

where the temperature T is in units of Kelvin and nanotube length L is in units of microns. The length dependence is based on Matthiessen's rule assuming an intrinsic mean free path of 500 nm. The thermal conductivity (k') is defined with a cross-sectional area of $A = \pi d\delta$ and the thermal conductance as plotted in Fig. 4 is calculated from this model as $G = k'\pi d\delta/L$. The majority of the molecular dynamics simulations are for nanotubes of slightly smaller diameter, $d \sim 1.4$ nm, than those of the measured CNTs, $d \sim 1.8$ nm. However, the results of the model of Che, Cagin, and Goddard, III (2000) for (10,10) SWCNTs ($d = 1.36$ nm) are included in Fig. 4. Above lengths of ~10 nm, the MD simulation reached a constant thermal conductivity and the conductance plotted in Fig. 4 is predicted from this value. The trend of the thermal conductance with length appears to agree well with several of the models, and this is perhaps surprising owing to the difference in CNT diameters. No experimental results are available for nanotubes shorter than ~0.5 μm and

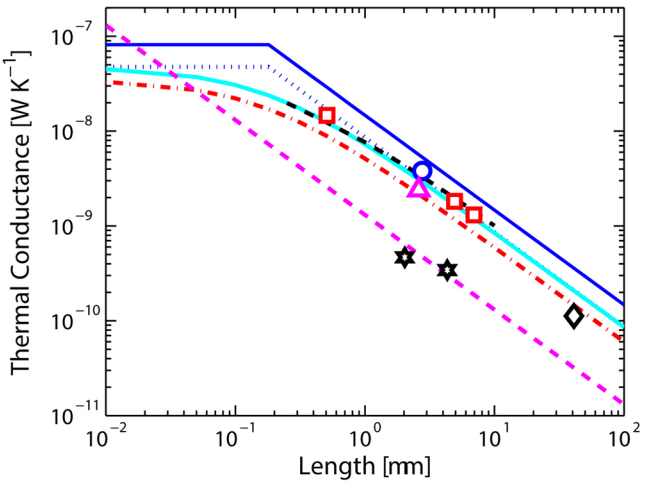

Article	Chirality	Diameter (nm)	Model or Experiment
Shang *et al.* (2007)	(24,0)	1.88	Ballistic Conductance Model
Shang *et al.* (2007)	(14,14)	1.89	Ballistic Conductance Model
Wang *et al.* (2006)	(14,14)	1.89	Ballistic-to-Diffusive Crossover
Wang *et al.* (2007a)	-	1.9	Wave Vector Model
Che *et al.* (2000)	(10,10)	1.4	Molecular Dynamics
Pop *et al.* (2006)	-	1.7	Empirical Model
Wang *et al.* (2007a; 2007b)	-	1.9	Experiment
Yu *et al.* (2005)	-	1 to 3	Experiment
Pop *et al.* (2006)	-	1.7	Experiment
Li *et al.* (2009)	-	1.8	Experiment

FIG. 4 (color online). Predictions and data for the thermal conductance of single-wall carbon nanotubes with comparable nanotube diameters. The models of Wang and Wang (2006), Shang, Ming, and Wang (2007), Wang, Tang, Zheng *et al.* (2007), and Wang, Tang, Li *et al.* (2007) were computed with nanotubes with ~1.9 nm diameter and for Wang and Wang (2006) and Shang, Ming, and Wang (2007) a mean free path of 180 nm was used in the calculations. For the empirical model of Pop *et al.* (2006), a phonon mean free path of 500 nm was extracted from experiments. The ballistic conductance models can be extended to any chirality of nanotube and to multiwall nanotubes; however, the model from Pop *et al.* (2006) was developed in conjunction with experimental data for thermal conductivity vs temperature, so is strictly only valid for nanotubes of the same diameter and chirality. For the wave vector model of Wang, Tang, Zheng *et al.* (2007), the Grüneisen parameter and the specularity of boundary scattering were adjusted to match the data from their experiment. The molecular dynamics simulation of Che, Cagin, and Goddard, III (2000) was computed only up to lengths of 50 nm, but above ~10 nm a uniform value of the thermal conductivity was achieved and that is what is plotted. All measurements and predictions are at room temperature.

the fully ballistic conduction regime is predicted at room temperature only for these short lengths.

In MD simulations, variations in the size of the simulation domain, i.e., the nanotube length, and in the boundary conditions at the ends of the simulation domain, can lead to differences in the predicted thermal conductivity. Periodic boundary conditions along the axis of the nanotube are used to approximate nanotubes of infinite length (Berber, Kwon, and Tománek, 2000; Zhang *et al.*, 2004). However, periodic boundary conditions do not accurately simulate long nanotubes. Zhong and Lukes (2004) and Lukes and Zhong (2007) reported that, even with periodic boundary conditions, increasing the simulated length of the nanotube increased the predicted thermal conductivity. Lukes and Zhong (2007) suggested that this arises from the fact that longer nanotubes have more vibrational modes with smaller wave vectors and longer wavelengths, which provide new pathways for heat transfer not captured by simulations with shorter period. The "new" low wave vector modes can be particularly effective contributors to the thermal conductivity since they are less likely to scatter due to umklapp processes. Finite lengths of the simulated nanotubes allow investigation of the size effect (Che, Cagin, and Goddard, III, 2000; Osman and Srivastava, 2001; Maruyama, 2002, 2003; Grujicic, Cao, and Gersten, 2004; Padgett and Brenner, 2004; Grujicic, Cao, and Roy, 2005; Zhang and Li, 2005; Zhang, Fan, and Yuen, 2006). Some simulations achieved convergence with length in as little as 10 nm (Che, Cagin, and Goddard, III, 2000; Grujicic, Cao, and Gersten, 2004; Grujicic, Cao, and Roy, 2005) to ~150 nm (Padgett and Brenner, 2004). In other MD simulations, no convergence is found within the range of lengths simulated [0.1 to 100 nm (Zhang and Li, 2005), 6 to 400 nm (Maruyama, 2002, 2003)] and a power law ($k \sim L^{\alpha}$) can be fitted to these simulated results. The exponent α ranged from 0.1 to 0.4 depending on the chirality and temperature of the simulated nanotube (Maruyama, 2002, 2003; Zhang and Li, 2005). However, in these simulations, the simulated CNT length is shorter than the expected mean free path and the conduction is not diffusive. The thermal conductivity may yet saturate if the simulation was carried out to longer lengths.

Divergence of the thermal conductivity with length was also predicted for low-dimensional lattices (Lepri, Livi, and Politi, 2003; Balandin, 2011) and observed in models for CNTs when only first-order umklapp scattering is considered. Wang and Wang (2006) found that the thermal conductivity followed two separate power laws for the ballistic regime and the diffusive regimes, with the $\alpha_{\text{ballistic}} > \alpha_{\text{diffusive}}$. At low temperatures and short lengths (ballistic conductance), the relationship trended toward the ballistic limit $k \sim L$. However, for longer nanotubes or at higher temperatures the tubes demonstrated more diffusive behavior, $k \sim L^{\alpha}$ with $\alpha > 1$. Solutions to the Peierls-Boltzmann equation (Mingo and Broido, 2005b) and wave vector models (Wang, Tang, Zheng *et al.*, 2007) have both shown that considering only first-order three-phonon processes leads to thermal conductivity diverging with length, but when three-phonon processes are included to second order, the thermal conductivity saturates with length agreeing better with experimental results. Yamamoto *et al.* (2009) discussed that when considering only first-order umklapp processes, the thermal conductivity diverges with length as $k \sim L^{1/2}$ due to the model for the acoustic phonon branches, but this can be corrected by considering higher-order scattering processes. However, Yamamoto *et al.* (2009) obtained good agreement between MD simulations and their model including only first-order umklapp processes indicating that, for the lengths considered, higher-order effects may be negligible.

In general, in the ballistic conduction regime, the thermal conductance is constant (i.e., the thermal conductivity increases with length), while in the diffusive conduction regime, the thermal conductivity saturates to a constant value. In the intermediate regime, a smooth transition results from quasiballistic or mesoscopic effects. Models which neglect higher-order three-phonon processes result in predicted

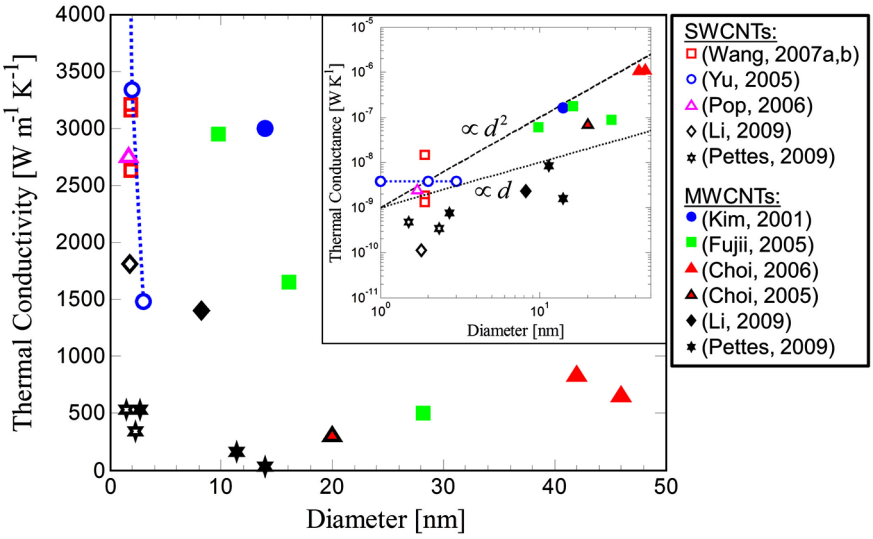

FIG. 5 (color online). Thermal conductivity data as a function of nanotube diameter. Open and solid data points are for single-wall and multiwall nanotubes, respectively. A decrease in thermal conductivity with increasing diameter is observed. The range of values shown for Yu *et al.* (2005) is due to the uncertainty in the measurement of the nanotube diameter. The SWCNT data for Pettes and Shi (2009) are a lower bound on the thermal conductivity, while the effect of contact resistance at the ends of the nanotubes is accounted for in the MWCNTs. Thermal conductivity values are standardized using the enclosed area of the nanotube $A = \pi d^2/4$. The inset shows the data for thermal conductance ($G = kA/L$) as a function of nanotube diameter. For illustration, the dashed and dotted black lines show $G \sim d$ and $G \sim d^2$, which relate to the two definitions of area typically used to define thermal conductivity from measurements and predictions of thermal conductance.

thermal conductivities which diverge with increasing length for all lengths, which is not physically observed. Additionally, MD models in which the domain is smaller than the mean free path exhibit increasing thermal conductivity. To accurately predict the thermal conductivity of long CNTs the models must be extended to longer lengths.

b. Chirality and diameter

While the dependence of the electrical properties on the chirality is well documented, the impact of chirality on the thermal properties has received less attention. Experimentally it is difficult to measure or control the chirality of the nanotube, although the outer diameter is typically measurable. In simulations, effects of both the diameter and the chirality can be explored, but many discrepancies exist between the results of different calculations.

Figure 5 shows experimental results of the diameter dependence of the room temperature thermal conductivity for both single-wall and multiwall nanotubes. For SWCNTs, the diameter dependence of the thermal conductivity is difficult to observe because most data are for tubes with similar diameters (1.7–1.9 nm). Yu *et al.* (2005) measured a nanotube which had a diameter in the range of 1–3 nm, but not exactly known due to the limits of the measurement technique, leading to the large range of thermal conductivities shown on the graph. Combining the SWCNT and the MWCNT data in the figure shows a general decrease in thermal conductivity with increasing diameter. Pettes and Shi (2009) found that the thermal conductivity of MWCNTs decreased with the number of walls, but this apparently correlated with an increased concentration of defects in nanotubes with more walls. Note, however, that the thermal conductance increases with diameter (see the inset of Fig. 5).

Many have shown through simulations of tubes with the same chirality that the thermal conductivity decreases with increasing diameter (Cao *et al.*, 2004; Chantrenne and Barrat, 2004; Zhang and Li, 2005; Wang and Wang, 2006; Yan, Xiao, and Li, 2006). The exact dependence of thermal conductivity on CNT diameter is due to a combination of the diameter dependence of scattering rates and change in number of conduction channels with tube diameter. For both armchair (n, n) and zigzag $(n, 0)$ nanotubes, Yan, Xiao, and Li (2006) calculated that $k \sim n^{-2}$ with the explanation that the increased phonon energy gap in smaller diameter nanotubes relaxes requirements for conservation of both energy and momentum, suppressing umklapp processes in small diameter nanotubes. The room temperature thermal conductivity of chiral nanotubes depends on the number of atoms in the unit cell N, which depends on the diameter, and the density of the nanotube ρ (Yan, Xiao, and Li, 2006):

$$\frac{k|_{T=300\ \mathrm{K}}}{\rho} \propto N^{-1.3}. \tag{23}$$

When comparing armchair nanotubes, Osman and Srivastava (2001) found that the smaller diameter nanotubes had the highest thermal conductivity compared to the larger nanotubes at room temperature. Wang and Wang (2006) found that the room temperature thermal conductance should follow the relationship $G \sim d$ for single-wall nanotubes. The diameter of a nanotube is given by Eq. (5), and for both armchair (n, n) and zigzag $(n, 0)$ nanotubes, the diameter of the nanotube goes as n. Thus, the thermal conductivity from Wang and Wang (2006) goes as n^{-1}, a slightly different dependence than from Yan, Xiao, and Li (2006) but agreeing with the general trend of the thermal conductivity decreasing with increasing diameter. Zhang, Fan, and Yuen (2006) and Qiu

et al. (2012) reported that the thermal conductivity of armchair and zigzag nanotubes at 300 K increased with increasing diameter from MD simulation results. Note that, for both of these cases, the reported conductivity values were calculated with $A = \pi d\delta$ and the trend with diameter reverses when the area $A = \pi d^2/4$ is used to calculate the thermal conductivity from the predicted thermal conductance. Nonetheless, in both cases, the thermal conductance ($G \sim kA$) increases with diameter.

Several simulations showed the peak in thermal conductivity with temperature shifts depending on nanotube diameter, although the direction of the shift is not consistent. Cao *et al.* (2004) and Yan, Xiao, and Li (2006) found that the temperature at which the thermal conductivity reaches its maximum value shifts to lower temperatures for larger diameter nanotubes. Cao *et al.* (2004) noted that this is because at all temperatures the probability of umklapp processes increases for larger diameter nanotubes. The geometry of one-dimensional systems reduces the number of states into which phonons can scatter and therefore in larger diameter tubes, there are more lower energy phonon states (Cao *et al.*, 2004). This is contrary to the argument of Osman and Srivastava (2001) that at all temperatures umklapp processes are more likely in smaller diameter nanotubes with minimum wave vectors closer to the reciprocal lattice vector. Osman and Srivastava (2001) predicted that the peak in thermal conductivity with temperature occurs at a lower temperature in smaller diameter nanotubes. Measurements of several different SWCNTs (Pop *et al.*, 2005, 2006; Yu *et al.*, 2005) and MWCNTs (Kim *et al.*, 2001; Fujii *et al.*, 2005) all show peaks in the thermal conductivity around 300 K regardless of diameter, suggesting that any shift in the peak with diameter is slight. Defects present in these measured nanotubes may be more important than the diameter and chirality determining the scattering rate and peak thermal conductivity (Mingo and Broido, 2005b).

Several modeled the effect of nanotube chirality on the thermal conductivity. Many found no major effect of the chirality on the thermal conductivity (Osman and Srivastava, 2001; Yamamoto, Watanabe, and Watanabe, 2004a, 2004b; Mingo and Broido, 2005a; Zhang and Li, 2005; Wang and Wang, 2006). The phonon density of states is not significantly altered for different chirality of nanotubes suggesting that the thermal conductivity should not be significantly affected by chirality (Yu, Kalia, and Vashishta, 1995; Zhang and Li, 2005). Yamamoto, Watanabe, and Watanabe (2004a, 2004b) found that the energy of the lowest optical phonon mode depended only on the nanotube radius, not the chirality.

Other modeling efforts reported thermal conductivity variations with chirality (Osman and Srivastava, 2001, 2005; Zhang *et al.*, 2004; Shang, Ming, and Wang, 2007), possibly due to the structural differences between the bonds in nanotubes of different chiralities. In armchair and chiral nanotubes, the sigma bonds form along the nanotube circumference, while in zigzag nanotubes, these bonds are along the nanotube axis. The stretching of the sigma bonds cause excess strain along the nanotube circumference, which shortens the mean free path of armchair and chiral nanotubes and lowers the thermal conductivity (Osman and Srivastava, 2001; Zhang *et al.*, 2004). In a MD simulation of the propagation of a heat pulse in a SWCNT, Osman and Srivastava (2005) found the amount of energy carried by the longitudinal acoustic and twist phonon modes is larger for zigzag than for armchair nanotubes. This finding agrees with models which show that the zigzag nanotubes have higher thermal conductivity than other chiralities. Zhang *et al.* (2004) found that below 400 K the thermal conductivity of the (20,0) zigzag nanotube is higher than the (11,11) armchair nanotube of nearly identical diameter, but both peak at the same temperature and approximately the same maximum thermal conductivity. At all temperatures, a (10,13) chiral nanotube had lower thermal conductivity than zigzag and armchair nanotubes with the same diameter. The fact that zigzag nanotubes may have more phonon channels than armchair tubes for the same diameter compared to armchair nanotubes is a possible explanation for the higher ballistic conductivity of zigzag tubes (Shang, Ming, and Wang, 2007). In contrast, Yan, Xiao, and Li (2006) found that armchair nanotubes had a larger room temperature thermal conductivity than zigzag nanotubes at the same diameters. There is not a clear consensus on the effect of chirality and diameter on CNT thermal conductivity.

2. Temperature dependence

Several competing processes contribute to the temperature dependence of thermal conductivity of carbon nanotubes. At low temperatures, heat transport is ballistic and the thermal conductance and the thermal conductivity increase linearly with temperature, a trend that is present also in the quantum of thermal conductance in Eq. (3) (Yamamoto, Watanabe, and Watanabe, 2004a, 2004b; Mingo and Broido, 2005a, 2005b; Wang and Wang, 2006). The ballistic regime is predicted up to 100 K for (10,10) nanotubes of moderate length (~ 1 μm) (Mingo and Broido, 2005b). As the temperature increases and additional phonon modes contribute, the total thermal conductivity increases along with the increase in specific heat (Yamamoto, Watanabe, and Watanabe, 2004a, 2004b). A peak in thermal conductivity with temperature is expected near room temperature (Berber, Kwon, and Tománek, 2000; Osman and Srivastava, 2001; Cao *et al.*, 2004; Zhang *et al.*, 2004; Zhang and Li, 2005; Zhang, Fan, and Yuen, 2006) due to competition between the excitation of more high-frequency phonons and the increased scattering rate (Zhang and Li, 2005). At higher temperatures, the thermal conductivity begins to decrease with temperature as scattering processes dominate. The measurements and predictions in the literature follow the basic temperature dependence in Table IV.

Below a few Kelvin, only the four acoustic modes described in Sec. II.A contribute to the thermal conductance. As the temperature increases from a few degrees Kelvin toward room temperature, phonon-phonon scattering remains negligible and boundary scattering governs the phonon mean free path. Using $k = \sum Cv^2\tau$, it is evident that thermal conductivity increases with temperature as the specific heat and number of phonon modes increases (Hone, 2001) and the scattering rate due to boundary scattering remains constant (Mingo and Broido, 2005a; Yan, Xiao, and Li, 2006). As shown in Fig. 6(a), the temperature at which the optical

TABLE IV. Temperature dependence of the thermal conductivity of carbon nanotubes. Experimental results for MWCNTs appear to follow similar trends with temperature as SWCNTs.

Regime	Conductivity dependence
Ballistic regime (very low temperature)	$k \sim T$; ballistic conductance
Intermediate	$k \sim$ specific heat; more phonon branches excited increasing the specific heat
Peak	Balance between increasing specific heat and increased scattering
Diffusive regime (high temperature)	$k \sim T^{-1}$; scattering processes dominate; second-order three-phonon scattering processes contribute as $k \sim T^{-2}$

modes begin to contribute to the thermal conduction depends on the energy gap of the lowest-lying optical mode ($\hbar\omega_{op}$), which in turn depends on the chirality and nanotube diameter (see Fig. 2). For individual SWCNTs, this transition from a one-dimensional to two-dimensional regime has been predicted to occur approximately at a temperature $T_{1D} \approx 2\hbar v/k_B d$, as the lowest-lying optical phonon subbands begin to be populated and contribute to the heat capacity (Benedict, Louie, and Cohen, 1996; Hone, Batlogg *et al.*, 2000). As shown in Fig. 6(b), when the temperature is normalized by the energy gap of the lowest-lying optical mode (defining $\tau_{op} = k_B T/\hbar\omega_{op}$), the predicted thermal conductance for all modeled CNTs collapses to a single curve, which at low temperature can be approximated as (Yamamoto, Watanabe, and Watanabe, 2004b)

$$\frac{G}{4G_{th}} \approx 1 + \frac{3}{\pi^2} e^{-1/\tau_{op}} \left(1 + \frac{1}{\tau_{op}} + \frac{1}{2\tau_{op}^2}\right). \tag{24}$$

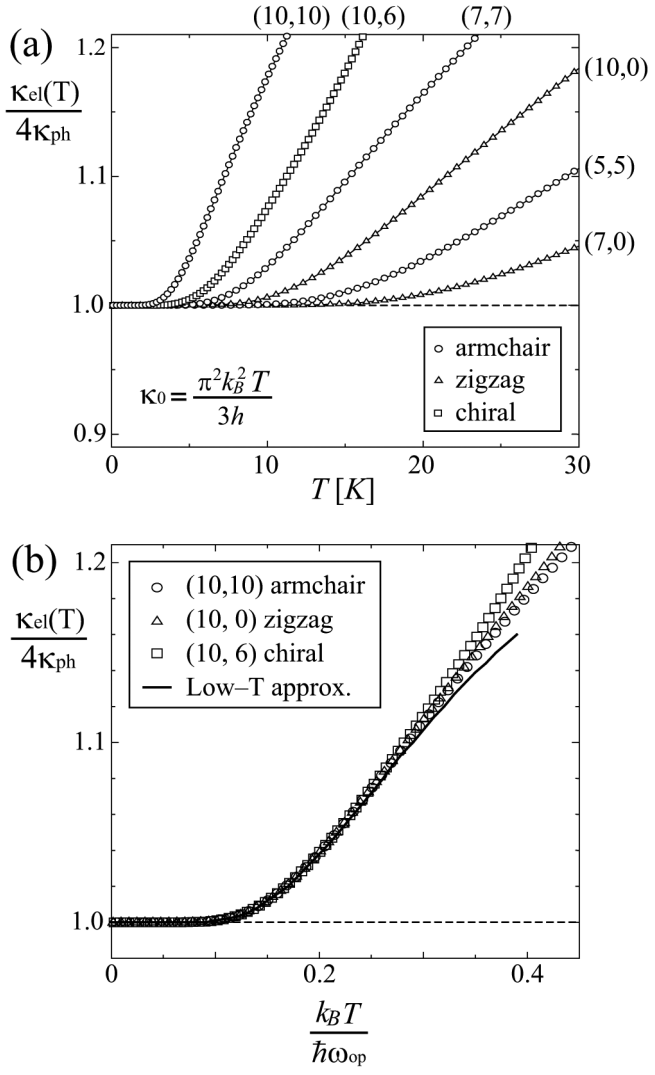

FIG. 6. (a) Low temperature thermal conductance of nanotubes with varying chirality as calculated by Yamamoto, Watanabe, and Watanabe (2004b). (b) When the temperature is scaled by the energy gap of the lowest optical mode, the thermal conductance for each of the different chiralities collapses to a single curve. From Yamamoto, Watanabe, and Watanabe, 2004b.

In the ballistic regime ($T < T_{1D}$), the heat capacity and thermal conductivity increase proportionally to temperature ($C \propto T$), but in this intermediate temperature regime, the specific heat and thermal conductivity increase more rapidly with temperature (Hone, Batlogg *et al.*, 2000; Dresselhaus *et al.*, 2004). Measurements of the specific heat of SWCNT bundles and models for isolated SWCNTs (Hone, Batlogg *et al.*, 2000) have shown that the specific heat deviates from the dependence above ≈ 8 K. First-principles density functional theory models (Kahaly and Waghmare, 2007) predicted that the thermal conductivity will follow the $T^{1.5}$ trend in heat capacity in this temperature range (up to ≈ 200 K). The measured thermal conductance of a SWCNT bundle showed a $T^{1.6}$ dependence from ≈ 15 to 50 K (Li, 2002). In contrast, the measured thermal conductivity of an individual 14 nm diameter MWCNT followed a $T^{2.01}$ dependence from 150 to 50 K and a $T^{2.50}$ dependence from 50 to 8 K indicative of the more two-dimensional behavior of MWCNTs (Kim *et al.*, 2001).

The thermal conductivity reaches a maximum when the increasing phonon population is balanced by reductions in the phonon mean free paths due to scattering. Several molecular dynamics (Osman and Srivastava, 2001; Zhang *et al.*, 2004; K. Zhang *et al.*, 2005) and lattice dynamic models (Cao *et al.*, 2004) found that the temperature at which the thermal conductivity achieves its maximum value depended on the nanotube chirality, with the peak conductivity in temperature in the range of 200 to 400 K. K. Zhang *et al.* (2005) found that the presence of isotope impurities modifies the temperature dependence of the carbon nanotube. Specifically, for a pure SWCNT, a peak in thermal conductivity was observed at 250 K, while when 40% ^{14}C impurity was introduced to the SWCNT model, the thermal conductivity decreased with increasing temperature from 100 to 400 K (K. Zhang *et al.*, 2005).

At higher temperatures, the thermal conductivity decreases with temperature as umklapp scattering processes dominate. First-order umklapp scattering processes lead to a $k \sim T^{-1}$ dependence at high temperature (Osman and Srivastava, 2001; Maruyama, 2003), but there is also a

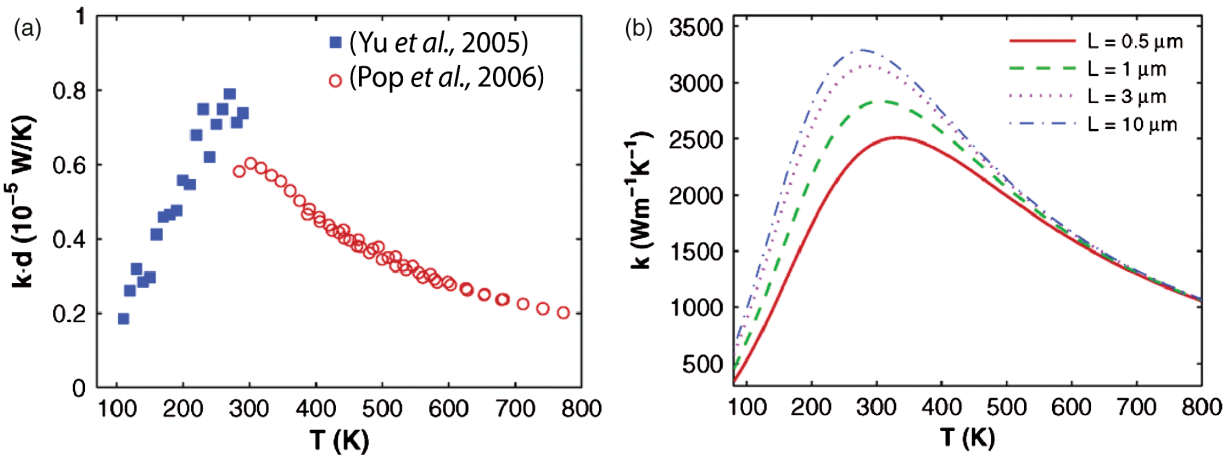

FIG. 7 (color online). (a) Diameter-adjusted CNT thermal conductivity as a function of temperature. Pop *et al.* (2006) used these data to calculate the empirical model of thermal conductivity with temperature shown in (b). (b) Thermal conductivity as a function of temperature using an empirical model based on experimental data in the left panel. From Pop *et al.*, 2006.

$\sim T^{-2}$ contribution due to second-order three-phonon effects (Pop *et al.*, 2006). Figure 7 shows both the combined experimental data set used for extracting the coefficients in the temperature-dependent thermal conductivity model [Eq. (22)] of Pop *et al.* (2006) and the resulting prediction of thermal conductivity at various lengths and temperatures.

Experimental results for MWCNTs appear to follow similar trends with temperature as those reported for SWCNTs. Kim *et al.* (2001) measured thermal conductivity of an individual multiwall carbon nanotube with temperature up to ~350 K. At low temperatures, from 8 to 50 K, the thermal conductivity increased with temperature as $k \sim T^{2.5}$. From 50 to 150 K, the thermal conductivity increased quadratically with temperature as $k \sim T^2$ agreeing with the predictions for two-dimensional conductors. The measured thermal conductivity peaked at ~3000 $\mathrm{W\,m^{-1}\,K^{-1}}$ at ~320 K and then decreased with temperature. Fujii *et al.* (2005) measured the thermal conductivity of three different diameter multiwall carbon nanotubes. For a multiwall carbon nanotube with a 16.1 nm outer diameter and a 4.9 nm inner diameter, the thermal conductivity increased from 100 to 320 K reaching a plateau or possible peak at 320 K.

3. Influence of defects

Molecular dynamics simulations enable systematic investigation of imperfect carbon nanotubes. Defects can arise from localized flaws in the atomic arrangement and from impurities. Using molecular dynamics simulations and atomistic Green's function analyses, several (Che, Cagin, and Goddard, III, 2000; Sevik *et al.*, 2011; Wang, 2011; Wei *et al.*, 2012) have shown that single vacancy, double vacancies, and Stone-Wales (5,7,7,5) defects significantly reduce the thermal conductivity, even at low defect concentrations. For example, Fig. 8 shows the predictions of Che, Cagin, and Goddard, III (2000) for the impact of common CNT defects in CNT including vacancies and the (5,7,7,5) defect, which changes the bond structure from four hexagons into two hexagons and two pentagons. For the (10,10) nanotube investigated, the thermal conductivity decreased by nearly a factor of 3 as defects of either kind are introduced into the system. The magnitude of the reduction is smaller for the (5,7,7,5) defect than for a vacancy because the basic bonding characteristic is not changed significantly. Similarly, using NEMD simulations, Sevik *et al.* (2011) predicted significant reductions in the thermal conductivity with the introduction of single vacancy, double vacancies, and Stone-Wales (5,7,7,5) defects in semiconducting (10,0) and metallic (10,10) SWCNTs. They found that the thermal conductivity saturated with increasing defect concentration above ~0.5% defects to ~160 $\mathrm{W\,m^{-1}\,K^{-1}}$ for all types of defects studied. Atomistic Green's function analyses (Sevik *et al.*, 2011; Wang, 2011) showed the transmission of high-frequency phonons through the defective CNTs is strongly suppressed. Specifically, the calculated mean free paths decayed proportional to ω^{-2}, characteristic of Rayleigh scattering in one-dimensional systems (Krumhansl and Matthew, 1965; Chaudhuri *et al.*, 2010).

Isotopic impurities also impact phonon transport within CNTs. K. Zhang *et al.* (2005) investigated the reduction in thermal conductivity due to the addition of ^{14}C and ^{13}C to a pure ^{12}C (5,5) single-wall nanotube [see Fig. 8(c)]. The thermal conductivity drops by more than a factor of 2 when 50% of the ^{12}C is replaced with ^{14}C and similar results were found for the ^{13}C impurities. The impurities also changed the temperature dependence of the thermal conductivity by impacting the phonon-phonon scattering mechanisms within the nanotube. Impurities can cause localization of high-frequency phonons, which can increase the contribution of low-energy, long wavelength phonons to conduction. Yamamoto, Sasaoka, and Watanabe (2011) simulated coherent phonon transport through isotopically impure CNTs of two chiralities [(5,5) and (8,0)] using nonequilibrium Green's function methods and observed three regimes of phonon transport (ballistic, diffusive, and localization regimes) dependent on the length of the nanotube relative to the frequency dependent phonon mean free paths and localization lengths. However, phonon localization may not have a measurable impact on thermal conduction compared to the impact of diffusive scattering. Using atomistic Green's function analysis of CNTs with random arrangements of isotopic impurities, Savić, Mingo, and Stewart (2008) predicted that the impact of phonon

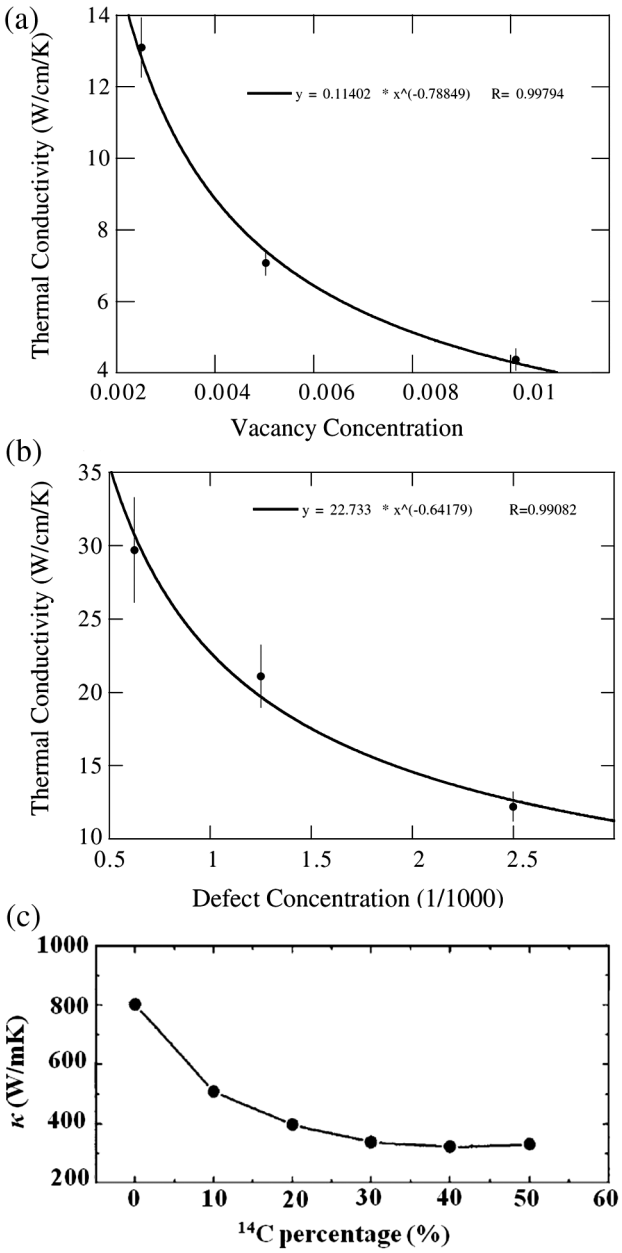

FIG. 8. Effects of defects on thermal conductivity. Effect of (a) vacancy and (b) (5,7,7,5) defect concentration from Che, Cagin, and Goddard, III (2000) using MD simulations. The solid lines are the best fit to the molecular dynamics simulations. (c) Effect of ^{14}C isotope impurity as computed by Zhang and Li (2005) using nonequilibrium molecular dynamics simulations.

localization should not be observable; rather the decrease in thermal conductivity in isotopically impure nanotubes is due to diffusive phonon scattering.

Although little theoretical work concerning defects has been conducted for MWCNTs, the results for SWCNTs suggest that defects should have a strong impact on MWCNTs as well. Additionally, it is predicted that although individual tubes in a defect-free MWCNT may act independently due to the weak interwall coupling, the presence of defects can cause scattering in all directions and link together different walls of the MWCNT (Yan, Xiao, and Li, 2006). Experimentally, Pettes and Shi (2009) observed no defects in single- and double-walled nanotubes using transmission electron microscopy, but the multiwalled tubes were found to have a high density of defects (30 to 77 dislocations per micron, increasing with the number of shells). The distance between defects (13 to 29 nm) correlated well with the estimated phonon mean free path within the MWCNTs (4 to 30 nm) (Pettes and Shi, 2009).

These theoretical and experimental studies show that defects can significantly impair thermal conduction, reducing it by more than one-half even at low defect densities. However, Ivanov *et al.* (2006) found that annealing a vertically aligned MWCNT array in argon at 2800° C for 2 h significantly reduced the sidewall defects increasing the thermal conductivity by up to a factor of 5 suggesting that postgrowth treatment of the carbon nanotubes could mitigate some of the impact of structural defects.

III. THERMAL CONDUCTION IN CARBON NANOTUBE ARRAYS AND MATS

Carbon nanotubes can be configured into a variety of materials including randomly oriented mats or vertically aligned arrays of nanotubes. Randomly oriented nanotube mats do not take full advantage of the high thermal conductivity along the axis of the nanotube and high inter-CNT contact resistance can prevent the mats from having high thermal conductivity. Materials with aligned CNTs can better take advantage of the high thermal conductivities of individual nanotubes reported in the previous sections. The conductivities of CNT materials are governed by the packing fraction of CNTs, boundary resistances between the nanotube array and the substrate or other material, and by damage or defects that may be present in the nanotubes as a result of fabrication details including compression. Accurate models for thermal conduction CNT networks require mesoscopic approaches which link thermal conduction in the individual nanotubes, CNT-CNT interactions, and realistic film morphologies. Furthermore, efficient thermal contacts to the CNT-based materials are critical for achieving high thermal conductivity.

A. Intrinsic film thermal conductivity

Randomly oriented CNT mats (also called bucky paper) typically show low thermal conductivity although the exact magnitude varies between reports. For example, for randomly oriented CNT films, Prasher *et al.* (2009) measured thermal conductivities on the order of 0.13 to 0.19 $W\,m^{-1}\,K^{-1}$, while Heo *et al.* (2011) reported values from 8 to 20 $W\,m^{-1}\,K^{-1}$. Magnetic alignment of carbon nanotube within the mats leads to improved room thermal conductivities from 40 200 $W\,m^{-1}\,K^{-1}$ along the direction of alignment and anisotropy ratios of ~3 to 9 (Hone, Llaguno *et al.*, 2000; Fischer *et al.*, 2003; Gonnet *et al.*, 2006). Drawing aligned MWCNT sheets and yarns from vertically aligned CNT (VACNT) arrays has also led to high thermal conductivity materials (50 and 26 $W\,m^{-1}\,K^{-1}$, respectively) (Aliev *et al.*, 2007). Inter-CNT contact resistance strongly impacts mat thermal conductivity and is discussed further in Sec. III.B.

Several research groups investigated and improved the thermal properties of vertically aligned CNT arrays for which the boundary resistance often dominates the total measured

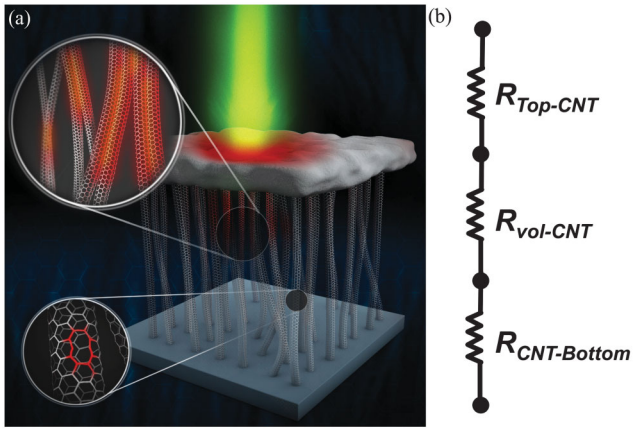

FIG. 9 (color). Schematic rendering of photothermal characterization and an approximate thermal resistance model for vertically aligned carbon nanotube films. (a) The rendering illustrates that a metal film is typically deposited on the top surface for heat absorption and thermoreflectance thermometry and suggests the importance of tube alignment, tube-tube interactions, and defects within tubes for transport in the film-normal direction. The quality of contact between the tubes and the metal film influences the extent to which heat penetrates into the film and can influence the experimentally observed effective heat capacity and complicate data extraction. (b) The series of resistances is a typical representation as used to model thermal transport across a CNT film in a configuration where the CNT film is in contact with two materials, including the thermal boundary resistance between the growth substrate and the CNT film ($R_{\text{CNT-bottom}}$), the volumetric thermal resistance of the CNT film ($R_{\text{vol-CNT}}$), and the thermal boundary resistance between the free surface of the CNT and the metals or other material deposited or placed on top of the CNT layer ($R_{\text{top-CNT}}$).

thermal resistance. Figure 9 shows a typical measurement configuration including a metal layer deposited on top of the CNT film. The total thermal resistance of the sample includes the thermal resistance between the CNT layer and its growth substrate, the volumetric thermal resistance of the CNT array, and the thermal resistance between the free surface of the CNT array and the top contact. We gathered thermal conductivity data from researchers whose experimental methods are designed to separate the volume and boundary resistances. This is a challenging task for data interpretation and has been achieved mainly using fast optical techniques including thermoreflectance [see, e.g., Yang *et al.* (2002) and Panzer *et al.* (2008)], photothermoelectric [see, e.g., Son *et al.* (2008)], photoacoustic [see, e.g., Cola, Xu, and Fisher (2007)], and laser flash [see, e.g., Xie, Cai, and Wang (2007)] methods. Effective thermal conductivities of vertically aligned CNT arrays reported in the literature span a large range from 0.145 $\mathrm{W\,m^{-1}\,K^{-1}}$ (Wang, Zhong, and Xu, 2005) to 267 $\mathrm{W\,m^{-1}\,K^{-1}}$ (Tong *et al.*, 2006, 2007). In some experiments it was not possible to separate the intrinsic thermal conductivity of the array from the boundary resistance. In these cases, the total resistance of the CNT array between two materials is reported (including both boundary resistances). Total thermal resistances ranged from 5 to 61 $\mathrm{mm^2\,K\,W^{-1}}$ (K. Zhang *et al.*, 2005; Xu and Fisher, 2006a, 2006b).

In an ideal array of vertically aligned CNTs, each individual CNT is straight, free of defects, and makes complete contact with both surrounding surfaces. In this case, the total conductance of the CNT array is the sum of the conductances of the individual tubes. In realistic arrays, incomplete contact of the CNTs to the surfaces reduces the number of CNTs contributing to heat conduction and forces heat to transfer between nanotubes. Additionally, defects and intertube contacts may increase the volumetric contribution to the thermal resistance. The measured or physical CNT thermal conductivity is related to the volumetric resistance by $k = L/R_{\text{vol-CNT}}A$, where the volumetric resistance includes the intrinsic thermal resistance due to the nanotube as well as the resistance due to defects and intertube contact resistances for heat transfer pathways involving multiple nanotubes.

If the nanotubes are assumed to function independently and all provide good contact to the top and bottom contacts, then the thermal conductivity for vertically aligned CNT films should scale linearly with the packing fraction. While the route to higher conductivity might appear to be increasing the packing fraction, this also increases the density of intertube contacts and the associated reductions in CNT thermal conductivity as discussed later in this section. While for randomly oriented nanotubes the contact points may provide a modest improvement in the conductivity by enabling additional heat flow paths, in general the contacts can be assumed to reduce the conductivity in aligned nanotubes owing to the reduced conductivity of the tubes. One exception to this argument is the situation when a small fraction of the nanotubes is in contact with an interface for which case the contact between nanotubes could diminish the effective thermal contact resistance.

Figure 10 shows the thermal conductivity of CNT samples as a function of the volume fraction CNTs. Data for individual nanotubes are represented at the right side of the plot where the volume fraction is unity. A simple estimate of the thermal conductivity of vertically aligned arrays of nanotubes k_{array} scales the thermal conductivity of individual nanotubes k_{CNT} by the volume fraction of CNTs ϕ:

$$k_{\text{array}} = \phi k_{\text{CNT}} = \frac{N_{\text{CNT}}}{A_{\text{array}}} A_{\text{CNT}} k_{\text{CNT}}. \tag{25}$$

For well-aligned CNT arrays, the volume fraction is equivalent to the area fraction and is calculated from the number of CNTs per unit area $N_{\text{CNT}}/A_{\text{array}}$. The theoretical thermal conductivity of a randomly packed bed of CNTs (modeled as large aspect ratio rods) is $k_{\text{mat}} = \phi k_{\text{CNT}}/3$ (Prasher *et al.*, 2009). There is some uncertainty in the reported values for the volume fraction for CNT films as it is difficult to measure accurately. Some report the number of tubes per unit area (for VACNT arrays as counted from microscope images), while in other cases the volume fraction is estimated from comparison of the density of a CNT array to the density of graphite.

The majority of the vertically aligned CNT samples discussed in the literature reported conductivities that fall well below predictions, indicated by the solid line in Fig. 10, considering 3000 $\mathrm{W\,m^{-1}\,K^{-1}}$ for an individual tube. Some samples correspond to individual nanotube thermal conductivities lower than 20 $\mathrm{W\,m^{-1}\,K^{-1}}$, indicating factors beyond the CNT density degrade the thermal performance of some

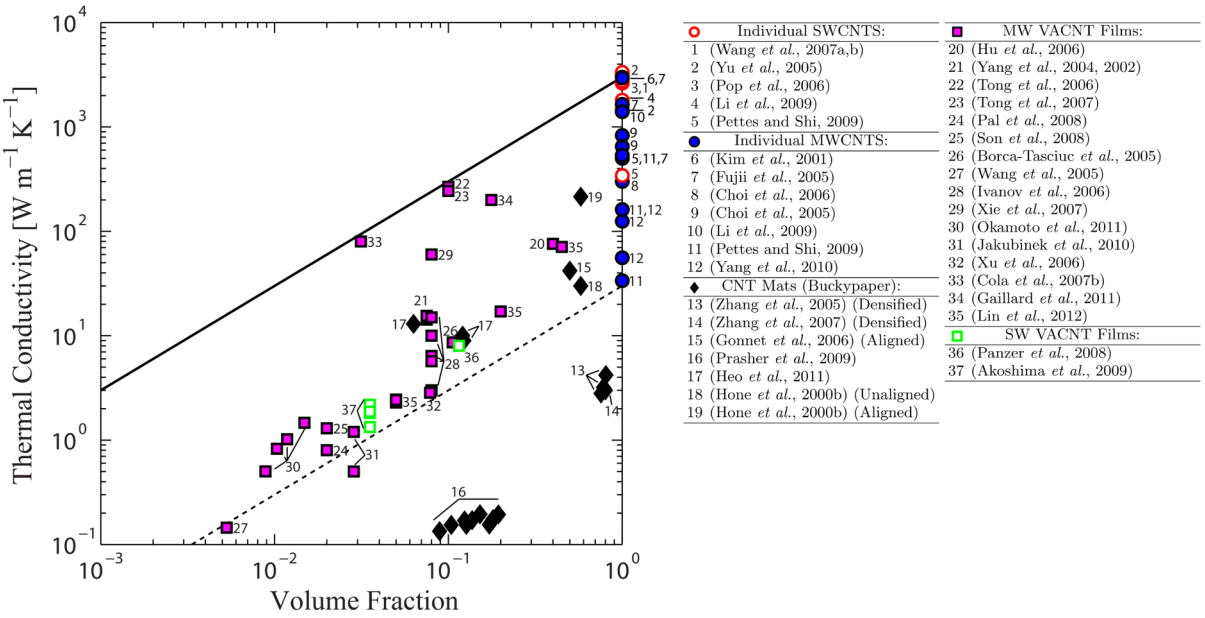

FIG. 10 (color online). Intrinsic thermal conductivity as a function of volume fraction for aligned CNT films and CNT mats. These data are for the intrinsic thermal conductivity of the films, which have been determined separately from the interface resistances. The solid line shows the predicted film thermal conductivity for an ideal array of nanotubes each with an individual thermal conductivity of 3000 W m^{-1} K^{-1}, while the dashed line shows the predicted film thermal conductivity with an individual CNT conductivity of 30 W m^{-1} K^{-1}. Individual nanotube thermal conductivities are provided on the left axis with volume fraction = 1. The volume fractions of aligned arrays range up to about 0.2, although unaligned densified arrays can achieve higher volume fractions. The densified arrays of H. L. Zhang *et al.* (2005) and Zhang *et al.* (2007) reported volume fractions of ~0.8–0.9 through spark plasma sintering of unaligned CNT mats. All of the nanotube arrays perform lower than predicted by the high thermal conductivity of individual nanotubes; however, recent data are approaching that limit as nanotube array fabrication improves and the resistances at the interfaces are addressed.

vertically aligned CNT arrays. For comparison, the dashed line in Fig. 10 indicates the predicted thermal conductivity for individual nanotubes within the arrays have thermal conductivity of 30 W m^{-1} K^{-1}. The high thermal conductivity (exceeding 250 W m^{-1} K^{-1} at ~10% volume fraction CNTs) reported by Tong *et al.* (2006, 2007) shows promise for fabricating vertically aligned CNT arrays which take full advantage of the high thermal conductivity reported for individual CNTs. The thermal diffusivity and thermal conductivity in aligned CNT arrays is highly anisotropic, such that the axial thermal conductivity is as much as 110 times greater than the radial conductivity (Borca-Tasciuc *et al.*, 2005; Ivanov *et al.*, 2006; Tong *et al.*, 2006, 2007; Son *et al.*, 2008).

Akoshima *et al.* (2009) reported a technique to reduce the distance between CNTs in freestanding SWCNT arrays increasing the density by a factor of 15 and leading to a significant increase in film thermal conductivity. For aligned densified MWCNT arrays infiltrated with epoxy, Marconnet *et al.* (2011) found that the thermal conductivity improved with increased CNT array density. However, the thermal conductivity did not follow the linear trend expected with volume fraction, nor did it increase as rapidly as expected if each CNT contributes with the thermal conductivity 1000 W m^{-1} K^{-1}. Lin *et al.* (2012) found that biaxial mechanical densification of VACNT films increased the thermal diffusivity by a factor of 3 for a ninefold increase in film density. Prasher *et al.* (2009) showed through modeling efforts that random mats of nanotubes are as thermally insulating as polymers. If the intertube contact resistance is high, the large number of tube-tube contacts in randomly oriented CNT films, or even poorly oriented VACNT arrays, would make any pathway for heat conduction involving multiple CNTs highly resistive.

Figure 11 shows the thermal conductance of an individual nanotube G_{CNT} extracted from measurements of arrays of nanotubes as a function of nanotube length:

$$G_{CNT} = \frac{k_{array}}{\phi}\frac{A_{CNT}}{L}, \tag{26}$$

where k_{array} is the measured thermal conductivity of the entire array, A_{CNT} is the cross-sectional area of an individual nanotube in the array, and L is the height of the nanotube array. The L^{-1} trend observable in Fig. 3 for individual nanotubes is also observed in the array data in Fig. 11 for lengths up to 1 mm, indicating that the thermal conductivity saturates with length. Above 1 mm, the introduction of defects during CNT growth may impede conduction. The differences between conductivities measured for individual nanotubes and those deduced from array data may result in part from differences in diameter or quality. For the MWCNT arrays, the diameters range from 10 to 200 nm, while in the measurements of individual of MWCNTs, the diameters varied from 8.2 to 46 nm. Within a single CNT array, there is a distribution of nanotube diameters.

Growth parameters, including the choice of substrate and adhesion layers on the substrate, deposition temperature, and catalyst material, govern the quality of the vertically aligned carbon nanotubes and therefore the thermal properties of the arrays. Typically thin films of titanium, aluminum, and nickel are deposited on silicon substrates for optimal CNT growth using chemical vapor deposition with methane as a carbon source (K. Zhang *et al.*, 2005; Hu *et al.*, 2006; Xu and Fisher,

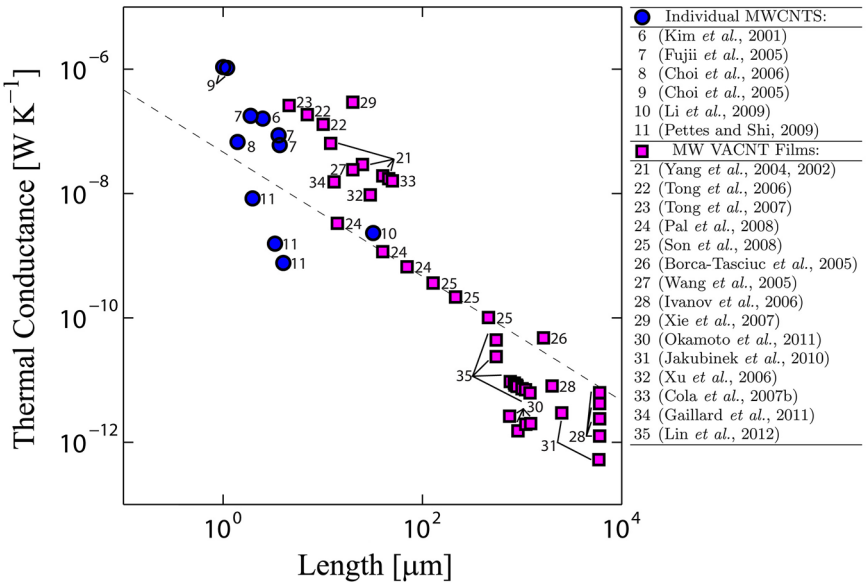

FIG. 11 (color online). Individual nanotube thermal conductances plotted as a function of nanotube length as extracted from reported measurements for arrays of MWCNTs and from measurements of MWCNTs. The dashed line shows L^{-1} trend of the thermal conductance which is expected if the thermal conductivity of a nanotube saturates at lengths longer than the mean free path.

2006a, 2006b). Titanium improves adhesion to the silicon substrate, while aluminum activates the nickel catalyst layer. The quality of the CNT growth, and the total thermal resistance of the sample, can depend strongly on the thickness of the aluminum layer and on whether the substrate annealed prior to CNT growth (K. Zhang *et al.*, 2005). K. Zhang *et al.* (2005) found that annealing the substrate before depositing the nickel catalyst was necessary to achieve vertically aligned CNT growth and the VACNT growth was further improved by annealing the substrate again after the catalyst deposition. Using a nickel catalyst layer, Yang *et al.* (2002, 2004) obtained vertically aligned CNT arrays without the titanium adhesion or aluminum activation layers. For their high thermal conductivity CNT films, Tong *et al.* (2006) used chemical vapor deposition with ethylene as a carbon source to grow the films on silicon wafers with a 10 nm aluminum film and 10 nm iron film as a catalyst. For some samples, an additional layer of molybdenum underneath the Al film improved adhesion. Cola, Xu, and Fisher (2007) grew high thermal conductivity arrays on successive layers of 30 nm titanium, 10 nm aluminum, and 3 nm of iron on copper films. Gao, Zhang, and Yuen (2011) controlled growth parameters including the number density of Fe catalyst nanoparticles, thickness of the catalyst layer, and carbon precursor flow rate to optimize the density and CNT alignment within their VACNT films and achieved low thermal resistance by optimizing optimized conditions. During microwave plasma chemical vapor deposition of MWCNT films, Cola *et al.* (2008) controlled the growth surface temperature and found that higher growth temperatures resulted in increased nanotube diameters and reduced thermal resistance (from 8 nm diameter and 19 mm^2 K/W at 500 °C to 40 nm diameter and 7 mm^2 K/W at 800 °C). Many other combinations of catalysts, substrates, and carbon sources are used to grow aligned carbon nanotube arrays.

The simulations and measurements of individual CNTs with defects discussed in Sec. II.D.3 showed that the thermal conductivity decreases significantly with increasing defect concentration. Assuming a fixed defect concentration, the probability of a defect occurring within a given CNT increases with the length, and thus arrays of longer tubes may exhibit a lower effective conductivity than shorter arrays of identical quality tubes. The study of growth kinetics of CNTs shows significant changes in CNT alignment and density with growth time within VACNT arrays (Bedewy *et al.*, 2009; Won *et al.*, 2012; Gao *et al.*, 2012). These effects could explain why the short nanotubes ($L < 10$ μm) of Tong *et al.* (2006, 2007) showed high film thermal conductivities, with the extracted individual nanotube thermal conductivity as high as 2650 W m^{-1} K^{-1}. As shown in Fig. 12, the individual CNT thermal conductivity (extracted from the effective

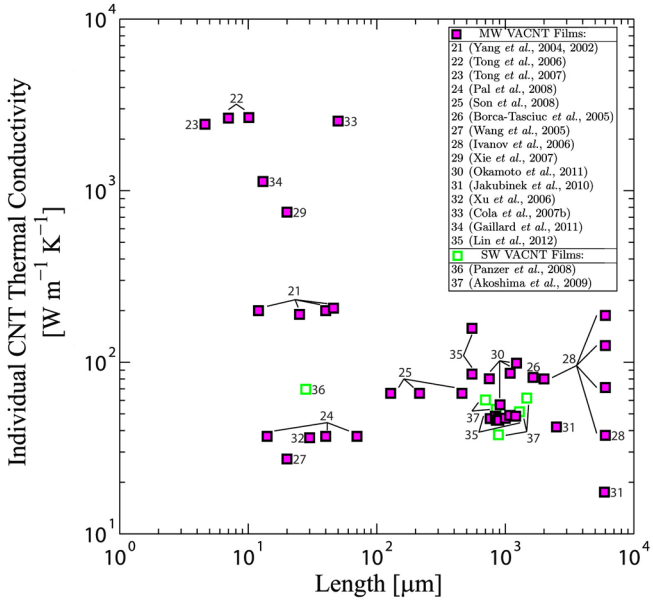

FIG. 12 (color online). Individual CNT thermal conductivities as a function of length extracted from reported data of the thermal conductivity or thermal conductance of CNT arrays.

arrays thermal conductivity and volume fraction) spans a large range at short film thicknesses and is generally lower for thick films. High temperature annealing of VACNT films [2 h at 980 °C in an Ar\H$_2$ (Lin *et al.*, 2012); 2 h at 2800 °C in an Ar (Ivanov *et al.*, 2006)] has been shown to improve the film thermal diffusivity likely due to annealing of defects within the nanotubes. While a factor of 8 increase in the Raman G/D band ratio and a factor of 3 to 5 improvement in thermal diffusivity was observed for annealing at 2800 °C (Ivanov *et al.*, 2006), only a 7% improvement in the G/D band ratio and 17% improvement in thermal conductivity was observed with the lower temperature anneal (Lin *et al.*, 2012). Furthermore, microwave annealing in air decreased the thermal diffusivity, possibly due to the introduction of oxygen-functionalized sites (Lin *et al.*, 2012). Although some compressive stress may improve contact between VACNT films and surrounding materials and between CNTs within the film and thus reduce the film thermal resistance [see, e.g., Cola, Xu, and Fisher (2007)], excessive compressive stress causes buckling of VACNT films and significant reduction in the film thermal conductivity (Lin *et al.*, 2012). A significant reduction (from 40 to 10 GW m^{-2} K^{-1}) in the thermal conductance of individual nanotubes with increasing buckling angle from 20° to 100° was predicted with MD simulations (Volkov *et al.*, 2012). Using mesoscopic models for the thermal conductivity of randomly oriented CNT mats, the film thermal reduced by ~20% when the impact of buckling on CNT conductance was included in the model (Volkov *et al.*, 2012). While experimental estimations of the mean free path of phonons in individual carbon nanotubes yielded values as high as 1.5 μm (Hone *et al.*, 1999; Yamamoto, Watanabe, and Watanabe, 2004a), the mean free path in films and bundles may be considerably shorter with corresponding lower thermal conductivity. Yang *et al.* (2002) estimated a phonon mean free path of only 20 nm in their multiwall nanotube arrays. The reduced mean free path could be a result of localized defects or tube-tube contact providing additional scattering sites for the phonon energy carriers. Chalopin, Volz, and Mingo (2008) modeled the effect of crossing nanotubes using molecular dynamics. The phonon transmission through a single-wall carbon nanotube was reduced very slightly when a second nanotube crossed it. For bundles of MWCNTs, Aliev *et al.* (2010) found that the thermal conductivity decreased by up to a factor of 4 relative to that of individual nanotubes. This suggested that within a single CNT certain phonon modes were suppressed as a result of contact and coupling with other nanotubes within the bundle (Aliev *et al.*, 2010).

B. Inter-CNT contact resistance

Thermal conduction within nanotube arrays and mats is complicated by the morphology of the nanotubes and the contact resistance between nanotubes. In randomly aligned mats, effective heat conduction through the mat is strongly dependent on efficient heat transfer between CNTs. For vertically aligned CNT films, although the CNTs generally span the entire thickness of the film, CNT-CNT contact resistance still plays an important role in thermal conduction through the film as CNTs.

Measuring the CNT-CNT contact resistance directly has proven challenging. Yang, Zhang, and Li (2010) experimentally measured the thermal contact resistance between crossing nanotubes using a method similar to the heater-sensor technique described in Sec. II.B for individual nanotubes. The contact resistance when two MWCNTs (of 74 and 121 nm diameter) crossed at nearly a 90° angle was 2 orders of magnitude larger than when two MWCNTs (170 nm and 165–185 nm diameter) contact in an aligned (parallel) configuration ($R''_{\text{CNT-CNT}} \sim 10^{-6}$ vs 10^{-8} W K^{-1}). When normalized by the contact area, the contact resistance is ~10^{-9} m^2 K W^{-1}. The contact resistance increased slightly as temperature decreased to 120 K. Below 120 K, the thermal contact resistance increased more rapidly ($R''_{\text{CNT-CNT}} \sim T^{-1.7}$ for 90° contacts and ~$T^{-2.4}$ for aligned contacts). Prasher *et al.* (2009) extracted an approximate CNT-CNT contact conductance of ~3 pW K^{-1} for contacting 1.4 nm diameter CNTs by fitting a model for thermal conduction in randomly oriented CNT mats to measured values of the film thermal conductivity. By scaling the conductance value from direct measurement of Yang, Zhang, and Li (2010) by the relative contact areas [(1.4 nm)^2/(74 nm × 121 nm)], the estimated contact conductance for 1.4 nm nanotubes is ~21 pW/K, slightly larger than that extracted from film measurement.

In part due to the challenge of accurately measuring the inter-CNT contact resistance directly, several modeling efforts have been conducted. Using both molecular dynamics and atomistic Green's function simulations, Prasher *et al.* (2009) found an interface thermal conductance of 50 pW K^{-1} for crossing SWCNTs. However, simulations using these models for individual tube-tube contacts overestimated the measured thermal conductivity of randomly oriented beds of CNTs, but are closer to the value estimated from the direct measurements of contact conductance (J. Yang *et al.*, 2010). Simulations of two nanotube junctions spaced more closely together than the coherence length of phonons within the CNTs yielded a contact conductance 1 order of magnitude smaller than that for a single junction and an overall thermal conductivity consistent with experiments (Prasher *et al.*, 2009). For all chiralities simulated, MD simulations by Chalopin, Volz, and Mingo (2009) showed that the interface thermal conductance was between 1 and 100 pW K^{-1} from 5 to 1000 K. Using MD simulations, Zhong and Lukes (2006) found that the thermal contact resistance between parallel (10,10) SWCNTs on the order of 10^{-7} m^2 K W^{-1}, while Maruyama *et al.* (2004) predicted a slightly smaller value of 6.48×10^{-8} m^2 K W^{-1} for parallel (5,5) SWCNTs. Zhong and Lukes (2006) predicted that thermal contact resistance decreased with increasing contact length (increasing contact area) and increased with increasing spacing between the two SWCNTs. As shown experimentally by J. Yang *et al.* (2010), MD simulations by Evans, Shen, and Keblinski (2012) showed that the thermal contact conductance for (10,10) SWCNTs depended strongly on the contact area, which is directly related to the angle at which the nanotubes cross. The extracted per area contact resistance of 7.7×10^{-9} m^2 K W^{-1} and the CNT-CNT contact conductance varied from ~600 for aligned contacts to ~100 pW K^{-1} for nanotubes crossing at a 90° angle. Increasing pressure increased the contact conductance for both aligned and crossed contact configurations as pressure increases the tube-tube van der Waals bonding stiffness and

the effective contact area increases as the tube deforms. Recent molecular dynamics simulations have shown that CNT-CNT contact resistance can be modified through the use of covalently bonded linker molecules such as CH_2 (Varshney, Patnaik, Roy, and Farmer, 2010).

In general, the high tube-tube contact resistance and modifications to the phonon modes limit the usefulness of randomly oriented CNT films for thermal applications. For comparison, measurements of the individual nanotubes yielded intrinsic thermal conductances ranging from 113 pW K^{-1} [41 μm long, 1.8 nm diameter SWCNT, (Li *et al.*, 2009)] to 1.08 μW/K [1 μm long, 46 nm diameter MWCNT (Choi *et al.*, 2006)] at room temperature (see Fig. 3 for a complete data set). A contact conductance of 21 pW K^{-1} (contact resistance $\sim 4.8 \times 10^{10}$ K W^{-1}) is equivalent to the thermal resistance of a $\sim$219 μm or 51.4 mm long CNT for these two values of intrinsic nanotube thermal conductance. These long equivalent lengths illustrate how, in randomly oriented CNT mats, efficient thermal conduction can be limited by the thermal conductance at the CNT-CNT interfaces. More work is needed in understanding the impact of CNT-CNT contacts in aligned CNT arrays where the CNTs span the entire film thickness. As mentioned in Sec. III.B, intertube contact may increase the thermal resistance of a CNT array by providing additional sites for phonon scattering or by damping phonon modes within a nanotube. As sketched in Fig. 13, the high CNT-CNT contact resistance combined with additional phonon scattering at contact sites may prevent the film thermal conductivity from achieving the performance expected from the high thermal conductance of individual nanotubes even in the aligned film configuration. The impact of CNT-CNT contacts may explain why the thermal conductivity of VACNT films often falls far short of that predicted by volume fraction (see Fig. 10).

C. Modeling of films and mats

Predicting the properties of bulk CNT films and mats requires models which take into account the morphology of the film or mat, entanglement, individual tube properties, and the impact of CNT-CNT contacts. Mesoscopic or hierarchical models which can take into account these factors are being developed to understand thermal transport in both aligned films and randomly oriented mats of CNTs.

Models for thermal conduction in CNT films span a range of complexities. Treating the CNTs as large aspect ratio rods, a rough approximation of the thermal conductivity of a randomly packed bed of CNTs can be estimated as $k_{\mathrm{mat}} = k_{\mathrm{CNT}}\phi/3$, where k_{CNT} is the individual CNT thermal conductivity (Prasher *et al.*, 2009). However, this estimate significantly overestimates the measured thermal conductivity of CNT mats due to the model neglecting the impact of thermal interface resistances between CNTs. Chalopin, Volz, and Mingo (2009) derived the randomly oriented CNT mat thermal conductivity considering the CNT-CNT contact resistance $R_{\mathrm{CNT\text{-}CNT}}$:

$$k_{\mathrm{mat}} = \frac{0.18L}{L_j^2} G_{\mathrm{CNT\text{-}CNT}} \approx \frac{0.18L}{2\pi D} \frac{\rho_{\mathrm{film}}}{\rho_{\mathrm{graphene}}} G_{\mathrm{CNT\text{-}CNT}}, \quad (27)$$

where $G_{\mathrm{CNT\text{-}CNT}}$ is the CNT-CNT contact conductance, L_j is the distance between CNT-CNT junctions, $\rho_{\mathrm{graphene}} = 7.6 \times 10^{-7}$ kg/m^2 is the surface mass density of graphene,

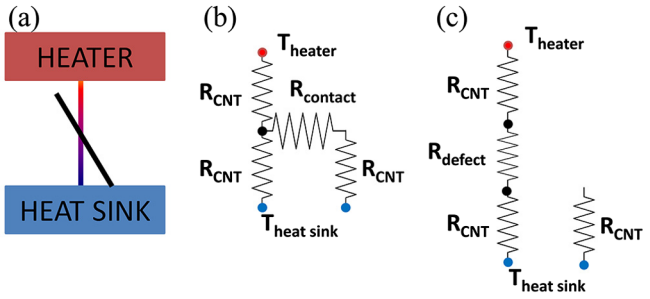

FIG. 13 (color online). (a) Schematic illustrating the conduction by two nanotubes in contact. In this example, one nanotube makes contact with both a heater and a heat sink. A second nanotube crosses the first but makes contact only with the heat sink. (b) Resistor network describing nanotubes in contact. While the second nanotube provides a second pathway for heat to transfer to the heat sink, the contact also provides a scattering site for the energy carriers. If the contact resistance is large, instead of aiding in the thermal conduction, the major effect of the second nanotube is to add a defect resistance to the conducting nanotube as modeled approximately by the extra resistor in the network in (c).

and ρ_{film} is the (volumetric) density of the randomly oriented mat, which can be estimated from $\rho_{\mathrm{film}} = \phi \times 2260$ kg/m^3. For several different CNT chiralities, combining their MD simulations for the CNT-CNT contact resistances with this approximation, Chalopin, Volz, and Mingo (2009) found the thermal conductivity in the dense limit is approximately 5 W m^{-1} K^{-1}. Volkov and Zhigilei (2010b, 2012) developed both analytical expressions and numerical models to predict the thermal performance of 2D and 3D randomly oriented CNT mats. Using a soft-core approach (Keblinski and Cleri, 2004), Volkov and Zhigilei (2010b) derived an expression for the 3D randomly oriented CNT film thermal conductivity assuming infinite nanotube thermal conductivity:

$$k_{\mathrm{mat}}^{\infty} = \frac{G_{\mathrm{CNT\text{-}CNT}}}{D} \frac{n_V^2}{18}, \quad (28)$$

where n_V is the volume number density of CNTs. They later extended this model to consider the finite thermal conductivity of the individual nanotubes and derived the following expression for the film thermal conductivity (Volkov and Zhigilei, 2012):

$$k_{\mathrm{mat}} = \frac{k_{\mathrm{mat}}^{\infty}}{1 + \mathrm{Bi}_c\langle n_j\rangle/12} = \frac{k_{\mathrm{mat}}^{\infty}}{1 + \mathrm{Bi}_T/12}, \quad (29)$$

where $\mathrm{Bi}_T = \mathrm{Bi}_c\langle n_j\rangle = G_{\mathrm{CNT\text{-}CNT}}\langle n_j\rangle L/kA$ is a Biot number comparing the total contact conductance from a nanotube to all of its contacts ($G_{\mathrm{CNT\text{-}CNT}}\langle n_j\rangle$) to the intrinsic nanotube thermal conductance (kA/L), and $\langle n_j\rangle$ is the average number of junctions per nanotube. Volkov and Zhigilei (2012) predict two limits to the film thermal conductivity: $k_{\mathrm{mat}} \propto \rho_{\mathrm{film}}^2 L^2$ when $\mathrm{Bi}_T \to 0$ and $k_{\mathrm{mat}} \propto \rho_{\mathrm{film}}$ when $\mathrm{Bi}_T \to \infty$. Although these relations differ from that of Chalopin, Volz, and Mingo (2009), they agree well with their mesoscopic numerical simulations of the CNT mats. The numerical simulations first model realistic randomly oriented CNT film geometry including effects stretching, bending, and buckling of the nanotubes and van der Waals interaction between tubes (Zhigilei, Wei, and Srivastava, 2005;

Volkov and Zhigilei, 2010a, 2010c). After generating the film geometry, the thermal conductivity was evaluated considering conduction within and between nanotubes (Volkov and Zhigilei, 2010b 2012). As opposed to the predictions of Chalopin, Volz, and Mingo (2009), Volkov and Zhigilei (2010b, 2012) showed that the mat thermal conductivity can span the range from thermal insulators to decent thermal conductors for a range of reasonable individual nanotube and nanotube contact properties. From the mesoscopic simulations, the distribution of the CNT-CNT contact conductances within the mat could also be evaluated. For a 0.2 $\mathrm{g\,cm^{-3}}$ dense mat consisting of 1 μm long (10,10) SWCNTs, the contact conductance had a broad distribution around a maximum of 257 $\mathrm{pW\,K^{-1}}$ and an average value of 1607 $\mathrm{pW\,K^{-1}}$. An intermediate value of $G_{\mathrm{CNT\text{-}CNT}} = 886.5\ \mathrm{pW\,K^{-1}}$ and $\langle n_j \rangle = 75.1$ leads to good quantitative agreement between Eq. (29) and the mesoscopic models. Experimental results for the thermal conductivity of randomly oriented CNT mats span several orders of magnitude from $<0.2\ \mathrm{W\,m^{-1}\,K^{-1}}$ (Prasher *et al.*, 2009) to over $30\ \mathrm{W\,m^{-1}\,K^{-1}}$ (Hone, Llaguno *et al.*, 2000) (see Fig. 10) illustrating that CNT mats can be tuned from thermal insulators to thermal conductors as predicted by the models of Volkov and Zhigilei (2010b, 2012).

Similar to randomly oriented mats, thermal conduction in aligned CNT films has been predicted through a number of models. As mentioned in Sec. III.A, simplified predictions of the performance of vertically aligned CNT films often consider the CNTs as thermal resistors in parallel and estimate the film thermal conductivity based on individual nanotube thermal conductivity and the film density [see Eq. (25)]. In reality, CNTs within a vertically aligned CNT film have a distribution of diameter, chirality, number of wall, length, and quality. Furthermore, the density and alignment vary along the thickness of the film. Several have studied the morphological variations and nonhomogeneities within CNT films (Zhang *et al.*, 2006; Bedewy *et al.*, 2009; Gao *et al.*, 2013). Briefly, these studies showed that often the VACNT growth consists of three stages: (1) the initial growth of a thin highly entangled crust layer, (2) steady film growth consisting of well-aligned nanotubes, and (3) CNT density decay as the catalyst layer is exhausted. The density decay at the film base can be avoided if film growth is terminated before the catalyst is completely consumed. Even in the main portion of the film with well-aligned nanotubes, CNT-CNT contacts, entanglement, and bundling of nanotubes impact thermal conduction. Mesoscopic models for aligned CNT films, similar to those of Volkov and Zhigilei (2010b, 2012) for randomly oriented mats, are required to fully model the interactions between the individual nanotube properties, film morphology including nonhomogeneous alignment, bundling, and entanglement, and CNT-CNT contacts on the film thermal conductivity. Theoretically, the models for randomly oriented nanotube mats should provide a minimum for the thermal conductivity in aligned films.

D. CNT-substrate thermal boundary resistance

Interface resistances play an important role in the thermal conduction through CNT arrays and can be the dominant source of resistance. These include the resistances of the growth interface with the substrate and with any films deposited or mechanically affixed after growth. The contact resistance at the interface between the nanotube array and the growth substrate was found to be quite low in the range of 0.022–0.03 $\mathrm{mm^2\,K\,W^{-1}}$ (Yang *et al.*, 2002; Wang, Zhong, and Xu, 2005) for CNTs grown on silicon. In other cases such as MWCNTs grown on SiO_2, the growth interface resistance has been larger, $\sim$50 $\mathrm{mm^2\,K\,W^{-1}}$ (Son *et al.*, 2008). When metals are deposited on the top surface of the array, or another material is brought in contact with the top surface of the array, the interface resistance of that interface tends to be significantly larger. For example, Tong *et al.* (2006) found a thermal resistance of 1.1 $\mathrm{mm^2\,K\,W^{-1}}$ between the CNT array and silicon growth substrate, but 11.1 $\mathrm{mm^2\,K\,W^{-1}}$ between the CNT array and the Cr and Au coated glass piece placed on the top surface. Attaching the CNTs to the SiO_2 substrate using 1 μm of indium significantly reduced the resistance of the CNT-glass interface to 0.29 $\mathrm{mm^2\,K\,W^{-1}}$ (Tong *et al.*, 2006), most likely due to increasing the engagement with the MWCNTs. Similarly, Cola *et al.* (2008) observed a temperature-dependent hysteresis of the thermal boundary resistance of SiC-MWCNT-Ag interfaces. Specifically, the total thermal resistance decreased after heating to 250 °C, possibly due to improved contact to the Ag resulting from thermally induced diffusion of Ag into the MWCNT array (Cola *et al.*, 2008). Several methods have been developed to bond CNT arrays to substrates other than their growth substrate. These include indium solder (Tong *et al.*, 2006, 2007), palladium thiolate (Hodson *et al.*, 2011), electrothermal (Aradhya, Garimella, and Fisher, 2008), and thermocompression (Johnson *et al.*, 2009; Cross *et al.*, 2010; Hamdan *et al.*, 2010) bonding techniques, all of which have shown significant improvement in the total thermal resistance compared to unbonded interfaces. The relative contributions of the free tip interface resistance, intrinsic film thermal resistance, and growth substrate interface resistance are compared in Fig. 14 for several CNT bonding configurations.

The roughness of the CNT array and contacting surfaces can make a difference in the fraction of CNTs which make contact with the surfaces. Incomplete contact at the interfaces of the CNT and substrate can reduce the effective volume fraction of CNT participating in heat transfer (Panzer *et al.*, 2008) and amplify the interface resistances at the nanoscale between individual CNTs and the substrates. The TEM image in Fig. 15 of a cross section of the metal-SWCNT interface reveals that near the interface there are an increased number of voids and lower volume fraction of CNTs compared to deeper within the array. The variations in CNT heights can lead to an increase in the apparent resistance of the array since a large fraction of tubes do not completely contact both the top metal and the substrate. Panzer *et al.* (2008) used a 10 ns thermoreflectance technique to extract the effective volume fraction of SWCNTs within an array which participates in heat transfer from the effective heat capacity of the film. During transient diffusion normal to the film, only those nanotubes in thermal contact with the top metal layer absorb heat and contribute to the experimentally observed heat capacity. They found an order of magnitude fewer nanotubes contribute to the thermal properties of the nanotube array ($2.5 \times 10^{15}\ \mathrm{m^{-2}}$) than the expected nanotube density

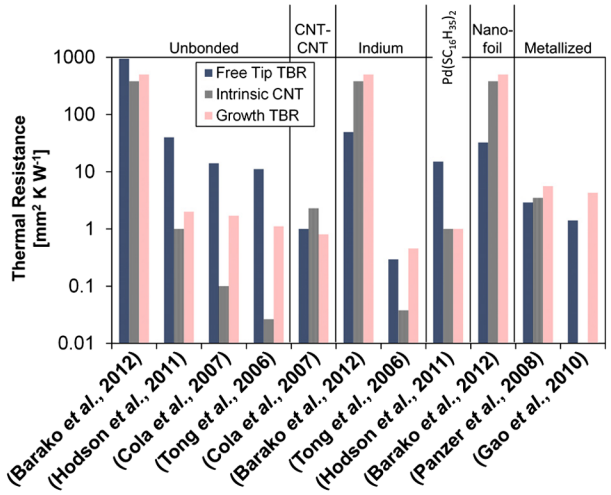

FIG. 14 (color online). Comparison of free tip thermal boundary resistance (TBR), intrinsic film thermal resistance, and growth interface thermal resistance for several CNT films. Several different free tip bonding configurations are compared: unbonded (dry) contacts, contact to a second CNT film (Cola *et al.*, 2007), indium solder bond (Tong *et al.*, 2006; Barako *et al.*, 2012), palladium thiolate bonding (Hodson *et al.*, 2011), reactive metal bonding (Barako *et al.*, 2012), and deposition of metal directly on the CNT free tips (Panzer *et al.*, 2008; Gao *et al.*, 2010). Generally the interface resistances exceed the intrinsic contribution from the CNT film.

based on the catalyst preparation (8.7×10^{16} m^{-2}) (Panzer *et al.*, 2008). Using the reduced CNT number density, the contribution to the thermal conductivity estimated for an individual nanotube in excellent contact with the interface was found to be ~2300 W m^{-1} K^{-1}. Many nanotubes make little contribution to the heat transfer. The thermal resistance of CNT arrays has been shown to decrease with applied pressure (Xu and Fisher, 2006a, 2006b; Cola *et al.*, 2007; Cola, Xu, and Fisher, 2007), most likely due to the effects of increasing the fraction of CNTs within the array contributing to heat conduction and increasing the real contact area (Xu and Fisher, 2006a; Cola, Xu, and Fisher, 2007).

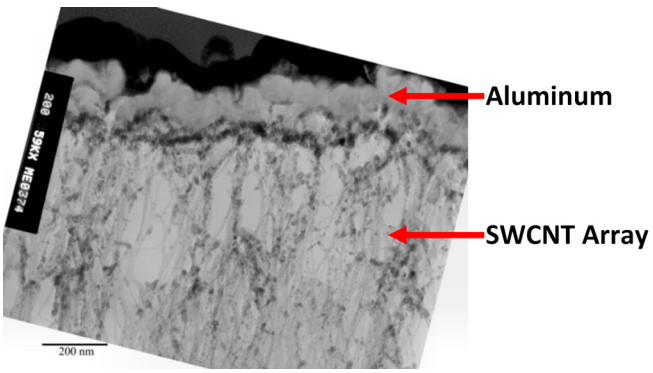

FIG. 15 (color online). Representative TEM of single-wall CNT array coated with a thin film of aluminum showing voids within the SWCNT array and, qualitatively, the regions of incomplete contact between the nanotubes with the aluminum layer. Adapted from Panzer *et al.*, 2010.

The interface between a CNT and a bulk medium differs from the standard contact between two bulk media as the carbon nanotube confined geometry exhibits may lead to quantum effects and this contact geometry requires new models to describe the conduction physics. Using a lattice dynamics approach, Panzer and Goodson (2008, 2011) studied the junction between 1D lattice and 3D face centered cubic lattice, as well as the junction between 1D and 2D square lattices. Even when two lattices have the same speed of sound, atomic spacing, and atomic mass, phonon transmission is impaired by the change in dimensionality. At room temperature, a maximum thermal conductance of ~100 pW K^{-1} was found by investigating several mass and stiffness ratios for a 1D-3D junction. While the 1D-3D model does not reproduce a CNT-substrate interface exactly, it suggests that phonon transmission across the interface will be dominated by the longitudinal phonons, while transverse and torsional phonons will have negligible contribution. Prasher, Tong, and Majumdar (2007) studied the thermal boundary conductance between a vertically aligned CNT array and a bulk substrate in the mesoscopic regime, for which the dominant phonon wavelength was of the order of the nanotube diameter, but shorter than the nanotube length. The dominant phonon wavelength ($\hbar v/\lambda_d \approx k_B T$) ranges from about 1 nm to several hundred nanometers depending on temperature for crystalline solids, while in carbon nanotubes it can be quite long even at moderately high temperatures (Prasher, Tong, and Majumdar, 2007). Assuming perfect transmission at the boundaries of a (6,0) SWCNT, at 100 K, ballistic conduction effects were predicted up to lengths of ~55 μm, while at room temperature ballistic conduction is predicted up to a length of 2.4 μm (Mingo and Broido, 2005a). Thus the interface consists of a 1D ballistic conductor in contact with a 3D bulk medium. Using a 3D vector elastic wave model, Prasher, Tong, and Majumdar (2007) studied the transmissivity and thermal conductance of (6,0) single-wall carbon nanotubes attached to a silicon substrate up to 55 K and found that the thermal conductance is several orders of magnitude less than that predicted with the assumption of perfect transmission at the boundaries.

While the above simulations were for CNTs attached vertically to a substrate, a horizontal configuration of the nanotube attached to the substrate is often more realistic. This horizontal contact configuration is often observed when CNTs are deposited on a substrate to form randomly oriented mats or single nanotube devices as well as due to bending of CNTs in vertically aligned films as they are brought into contact with a secondary substrate. Using MD, Ong and Pop (2010) estimated a thermal contact conductance of ~0.1 W m^{-1} K^{-1} for a 1.7 nm diameter SWCNT lying on a SiO_2 substrate and the contact conductance per unit area for all diameters simulated was $\sim 5.8 \times 10^7$ W m^{-2} K^{-1} at room temperature. The predicted contact conductance increased with diameter, van der Waals interaction strength (X), and temperature. Specifically, they found that $G_{\text{CNT-SiO}_2} \sim dXT^{1/3}$ where the $T^{1/3}$ dependence is indicative of inelastic phonon scattering at the interface (Ong and Pop, 2010). Several experimental works (Pop *et al.*, 2007; Pop, 2008; Shi *et al.*, 2009; Steiner *et al.*, 2009) considering CNTs on SiO_2 have shown this value of CNT-SiO_2 thermal contact

conductances is reasonable although the experimental values span a range from 0.007 to 0.20 $W m^{-1} K^{-1}$. Exact comparison of the experimental and theoretical results is challenging due to variations in nanotube diameter and experimental uncertainty. Maune, Chiu, and Bockrath (2006) experimentally estimated a thermal contact conductance of $\sim$0.3 $W m^{-1} K^{-1}$ for a CNT grown on a sapphire substrate. From the measurement of an individual 14 nm diameter MWCNT lying on a metal electrode (Kim *et al.*, 2001), the contact conductance per unit length is estimated to be 0.5 $W m^{-1} K^{-1}$ and the contact conductance per unit area is estimated to be 35 $MW m^{-2} K^{-1}$.

IV. APPLICATIONS

Individual carbon nanotubes as well as films and mats of CNTs have shown promise in a variety of applications (Baughman, Zakhidov, and de Heer, 2002; Ren, Lan, and Wang, 2013). This section highlights a few key applications where the thermal properties of CNTs provide advantages over conventional solutions.

A. Thermal interface materials

For many applications including electronics packaging, vertically aligned CNT arrays are promising as thermal interface materials and the total thermal resistance is a critical metric of their performance. The total resistance of a thermal interface material (TIM) includes both boundary resistances and the intrinsic thermal resistance. Optimal thermal interface materials also benefit from a variety of other attributes including a low elastic modulus E, which helps accommodate mismatch in the coefficient of thermal expansion between the hot surface and the heat sink. Conventional thermal interface materials include greases, gels, phase change materials, and metallic solders. Polymeric thermal greases have a relatively high thermal resistance, but have low elastic modulus. In contrast, metallic solders have lower thermal resistance but have much higher stiffness. Figure 16 compares thermal resistance data for CNT films with conventional TIM materials, showing that the total thermal resistance of CNT arrays can be better than thermal interface greases and even approaches those of metallic solders. The solid line in the figure shows that an ideal CNT array with 3% volume fraction and negligible boundary resistance could achieve lower thermal resistance than metallic solders of the same thickness. The extremely low CNT density and large aspect ratio of individual CNTs in bulk CNT films provides the possibility that the CNT array could have lower elastic modulus than even the conventional greases, making them promising for thermal interfaces. Recent work used a microfabricated silicon resonator to measure the in-plane modulus of aligned MWCNT films, yielding values between 10 and 500 MPa that are well below those of conventional interface materials (Won *et al.*, 2012). For use as TIMs, VACNT films can be grown directly on the device or heat sink and bonded at the free tip interface to the alternate material or the VACNT films can be grown on sacrificial substrates and bonded at both interfaces. Film

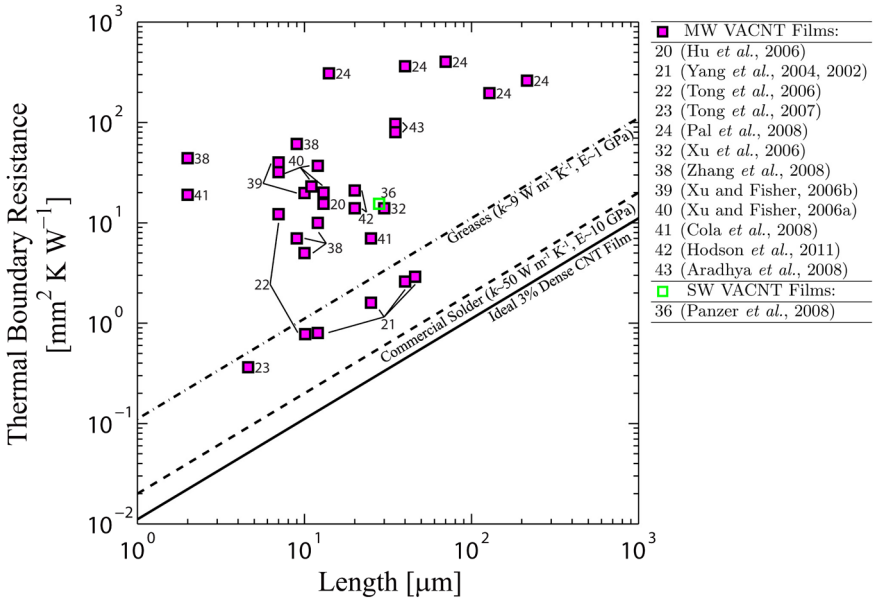

FIG. 16 (color online). Total thermal resistance of CNT arrays plotted according to length. The total thermal resistance includes the thermal boundary resistance between growth substrate and CNT film, the intrinsic thermal resistance of the CNT film, and the thermal boundary resistance between the free surface of the CNT and the metals or other material deposited or placed on top of the CNT layer. The solid line shows the lower limit for the thermal resistance of a CNT array at a packing density of 3% if each individual CNT has a thermal conductivity of 3000 $W m^{-1} K^{-1}$ and the thermal boundary resistance is negligible. The dot-dashed line shows an approximate lower bound on thermal resistance of commercial thermal greases used for thermal interface materials. Thermal greases and phase change materials have low thermal conductivities (on the order of 0.1–10 $W m^{-1} K^{-1}$). The dashed line shows the approximate thermal resistance of commercial alloy solders. Metallic solders have higher thermal conductivities (on the order of 40–90 $W m^{-1} K^{-1}$). Some of the best data for CNT arrays as thermal interface materials have achieved total thermal resistances less than commercially available greases, gels, and phase change materials and approaching that of metallic solders.

growth and bonding conditions (temperatures, pressures, etc.) must be controlled to avoid damage to the device during film growth and bonding.

B. Electrical interconnects

As transistor size reduces, the dimensions of the metallic interconnects within the computer chip architecture must also shrink. As the interconnect dimensions shrink, the electrical resistivity of conventional copper interconnects increases due to electron scattering and the lifetime of the interconnect reduces due to electromigration (Li *et al.*, 2004; Josell, Brongersma, and Tkei, 2009). Carbon nanotubes offer an attractive solution to the electrical challenges as well as providing a heat conduction pathway within the chip. Specifically, individual single-wall CNTs can be metallic or semiconducting based on chirality, which depends on the catalyst and growth conditions. Metallic CNTs have electrical conductivities greater than or equal to metals (McEuen, Fuhrer, and Hongkun, 2002). Additionally, individual CNTs have been shown to withstand large electric current densities ($>10^9$ A/cm^2) (Wei, Vajtai, and Ajayan, 2001). Individual CNTs, bundles of CNTs, and patterned arrays of aligned CNTs are good candidates for electrical interconnect applications (Naeemi, Sarvari, and Meindl, 2007; ITRS, 2011; Bhattacharya, Amalraj, and Mahapatra, 2011; Chow *et al.*, 2012). However, there are several key challenges for practically implementing CNT-based interconnects ranging from the selective growth of metallic SWCNTs to the compatibility of the CNT growth processing within the current complementary metal-oxide semiconductor and back end of the line processing (ITRS, 2011).

C. Individual nanotube devices

Carbon nanotubes have proven promising for numerous electronic and optoelectronic devices (Avouris, 2002; Avouris, Chen, and Perebeinos, 2007; Li *et al.*, 2010). Carbon nanotube field-effect transistors (Tans, Verschueren, and Dekker, 1998) have been integrated together to form logic gates and ring oscillators [see, e.g., Javey *et al.* (2002)]. Heat dissipation within single nanotube (and other nanoscale) devices is critical to their performance and reliability (Pop, 2010). Recently, scanning Joule expansion thermometry of SWCNT-based transistors has shown that chirality, diameter, and point defects impact the temperature profile within the device (Xie *et al.*, 2012). Effective heat dissipation along the nanotubes and from the nanotubes to the substrate is critical to developing and improving CNT-based electronic devices.

Recent experimental (Baloch *et al.*, 2012) and theoretical (Rotkin *et al.*, 2009) work suggested that electrical Joule heating of a CNT on a polar substrate may remotely heat the substrate, possibly due to surface phonon-polariton (SPP) interactions. Specifically, Baloch *et al.* (2012) observed that when the current was passed through a MWCNT deposited on a SiN membrane, the apparent temperature rise in the surrounding membrane was consistent with >84% of the applied power being deposited directly in the SiN membrane as opposed to traditional Joule heating within the CNT. Rotkin *et al.* (2009) predicted that heat dissipation due to the SPP interaction is significant compared to CNT-substrate thermal conductance and increases the effective CNT-substrate thermal conductance by an order of magnitude. Theoretically, SPP scattering has been shown to impact the electrical mobility and drift velocity within a CNT (Perebeinos *et al.*, 2009; Steiner *et al.*, 2009) and contribute to the effective temperature of the nanotube and substrate (Rotkin *et al.*, 2009; Steiner *et al.*, 2009).

D. Thermal rectification

Thermal rectification, which is a phenomenon where heat is conducted more or less easily depending on the direction of heat transport (i.e., positive or negative thermal bias), has been of interest for many decades (Roberts and Walker, 2011). Consider a single carbon nanotube stretched from between two heater or sensor elements as shown in the left panel of Fig. 1. If the nanotube exhibited strong thermal rectification, then, for example, heat would conduct easily (high conductance) when the left side is heated, but the nanotube would be thermally resistive (low conductance) when the right side was heated. The thermal rectification factor is defined as

$$\Re = \frac{J_+ - J_-}{J_-} \times 100\% = \frac{G_+ - G_-}{G_-} \times 100\%, \tag{30}$$

where J_+ and J_- and G_+ and G_- are the heat fluxes and thermal conductances under positive and negative thermal bias, respectively.

Recent experiments have shown that carbon nanotubes, as well as boron nitride nanotubes, loaded with varying thicknesses of $C_9H_{16}Pt$ along their length have shown thermal rectification. The rectification coefficient was $\Re \approx 2\%$ for CNTs and $\Re \approx 3\%$ to 7% for boron nitride nanotubes with better thermal conduction observed in the direction from the high to the low mass regions (Chang *et al.*, 2006). However, MD simulations of (10,10) carbon nanotubes with extra atoms gradually added along the length of the tube (Alaghemandi *et al.*, 2009) show rectification with the opposite sign: thermal conductivity is larger in the direction of low to high mass than the opposite direction. Similarly, MD simulations of a (10,10) nanotube with varying atomic mass (from 12 to 300) along its length have also shown thermal rectification ($\Re \approx 10\%$ at 300 K), with better conduction when the heat flux is in the direction from low to high mass (Alaghemandi *et al.*, 2009). Furthermore, MD simulation nanotubes with varying diameter (Wu and Li, 2008; Yang, Zhang, and Li, 2008) along their length, as well as defective CNTs (Takahashi, Inoue, and Ito, 2010), have shown evidence of thermal rectification.

In addition to thermal rectification in the axial direction, MD simulations of heat transport between the walls of double-walled CNTs have shown thermal rectification is possible in the radial direction (Bui *et al.*, 2012). Specifically, the thermal resistance from the heated outer shell to the inner shell was smaller than that from a heated inner shell to the outer shell due to differences in the

expansion and coupling between the shells upon heating. The rectification factor ranged from 103% to 114% depending on the shell chiralities (Bui *et al.*, 2012).

V. CONCLUSIONS AND OUTLOOK

In the last two decades, thermal conduction in CNTs has been investigated through the modeling and experimental efforts of many researchers. The high thermal conductivities of CNTs combined with their electrical and mechanical properties can yield bulk CNT materials with interesting and unique combinations of properties. Understanding thermal conduction in individual nanotubes is necessary for understanding the thermal conduction in bulk CNT materials.

Depending on growth parameters, the diameter, chirality, length, and quality of CNTs can vary significantly impacting the thermal conduction properties. While it is possible to model the effect of chirality and diameter, it is challenging to determine the chirality of nanotubes experimentally and there is no clear trend of thermal conductivity and diameter consistent between the different models. Experiments show that the thermal conductance generally increases diameter, although the thermal conductivity (using $A = \pi d^2/4$) decreases with diameter. Nanotubes can be grown with lengths exceeding several millimeters, which is much longer than the phonon mean free path. While several models have been developed for ballistic conduction appropriate for nanotubes shorter than the mean free path, the majority of CNTs and CNT films experimentally characterized are diffusive thermal conductors at room temperature and the thermal conductivity is independent of length. Several models showed that defects including vacancies, changes to the bond structure, and impurities significantly reduce the thermal conductivity of individual nanotubes. Experimentally it is difficult to directly observe and isolate the impact of defects. Ivanov *et al.* (2006) found that the thermal conductivity of bulk CNT arrays increased after annealing at high temperatures, possibly due to the reduction in the number of sidewall defects observed with high resolution TEM. Pettes and Shi (2009) found that for individual nanotubes the thermal conductivity decreased with increasing defect concentrations. To ensure high thermal conductivity of bulk CNT materials, high quality CNTs are required.

The thermal resistances for both CNTs and bulk CNT materials have two components: the intrinsic thermal resistance of the nanotubes and the thermal boundary resistance between the nanotubes and surrounding materials (i.e., substrate, deposited layers, etc.). For individual CNTs, the intrinsic thermal resistance must be optimized by controlling the growth quality and considering effects of geometry. In CNT mats, the high resistance between tubes limits the thermal conductivity of the film. In bulk aligned CNT materials, increasing the CNT volume fraction generally decreases the intrinsic thermal resistance of the material by increasing the number of nanotubes per unit area. As the intrinsic thermal conductivity of VACNT arrays has been improved through optimization of growth parameters, the limiting factor in implementing CNTs in practical applications is the high thermal boundary resistance between CNTs and surrounding materials. Reducing the thermal boundary resistance and increasing the fraction of CNTs contributing to the heat conduction is necessary for creating CNT films with desirable thermal properties.

Although much theoretical and experimental progress has been invested on understanding the physical mechanisms governing heat conduction by carbon nanotubes and related films, several questions and challenges remain. First, significant variations remain between the thermal properties measured for CNT samples from different research groups. While these variations arise in part from documented differences of geometrical parameters, such as diameter and CNT film density, the impact of defects for nanotubes and films with similar geometrical features needs more attention. Second, in order to apply CNTs and related materials to more applications, consistent and repeatable thermal properties must be demonstrated in samples that have been produced by batch or large-scale fabrication methods. Third, effective and reproducible thermal contacts to the CNTs are required to take advantage of the high thermal conductivity of individual carbon nanotubes in real applications. This can be assisted through improved understanding of the mechanisms of interfacial transport, which could lead to new strategies for minimizing the interface resistances. While recent simulations and experiments have improved the understanding of the thermal transport at interfaces between contacting CNTs, as well as between CNTs and bulk materials, open questions remain regarding transmission of vibrational modes and the impact of near-interfacial imperfections and disorder. Finally, more work is needed to explore novel three-dimensional nanostructures, which leverage the properties of CNTs and other carbon allotropes, which may provide unique multidimensional transport properties. For instance, graphene sheets interconnected with CNT pillars are expected to yield high values for both in-plane and cross-plane thermal conductivity (Varshney, Patnaik, Roy, Froudakis, and Farmer, 2010). A key challenge for these complex structures is the development of mesoscopic modeling techniques, which leverage more fundamental thermal models for individual nanotubes and interfaces into complex networks of relevance for applications.

ACKNOWLEDGMENTS

We gratefully acknowledge the financial support from the ONR (N00014-09-1-0296-P00004, Mark Spector, program manager), the NSF-DOE thermoelectrics partnership (CBET0853350), the National Science Foundation Graduate Research Fellowship program, and the Stanford Graduate Fellowship program. We also thank Chuan Hu and Intel for preparing the TEM image in Fig. 15 and Alex Jerez for the schematic rendering in Fig. 9. We acknowledge valuable technical discussions with Michael Barako, Yuan Gao, Chuan Hu, and Bo Qiu.

REFERENCES

Akoshima, M., K. Hata, D. N. Futaba, K. Mizuno, T. Baba, and M. Yumura, 2009, Jpn. J. Appl. Phys. **48**, 05EC07.

Alaghemandi, M., E. Algaer, M. C. Böhm, and F. Müller-Plathe, 2009, Nanotechnology **20**, 115704.

Aliev, A. E., C. Guthy, M. Zhang, S. Fang, A. A. Zakhidov, J. E. Fischer, and R. H. Baughman, 2007, Carbon **45**, 2880.

Aliev, A. E., M. H. Lima, E. Silverman, and R. H. Baughman, 2010, Nanotechnology **21**, 035709.

Aradhya, S. V., S. V. Garimella, and T. S. Fisher, 2008, in *Proceedings of the 11th Intersociety Conference on Thermal and Thermomechanical Phenomena in Electronic Systems (ITHERM 2008)* (IEEE, New York), pp. 1071–1077 [DOI: 10.1109/ITHERM.2008.4544381].

Avouris, P., 2002, Chem. Phys. **281**, 429.

Avouris, P., Z. Chen, and V. Perebeinos, 2007, Nat. Nanotechnol. **2**, 605.

Balandin, A., 2011, Nat. Mater. **10**, 569.

Baloch, K. H., N. Voskanian, M. Bronsgeest, and J. Cumings, 2012, Nat. Nanotechnol. **7**, 316.

Barako, M. T., Y. Gao, A. M. Marconnet, M. Asheghi, and K. E. Goodson, 2012, in *Proceedings of the 13th Intersociety Conference on Thermal and Thermomechanical Phenomena in Electronic Systems (ITHERM 2012)* (IEEE, New York), pp. 1225–1233 [DOI: 10.1109/ITHERM.2012.6231562].

Baughman, R. H., A. A. Zakhidov, and W. A. de Heer, 2002, Science **297**, 787.

Bedewy, M., E. R. Meshot, H. Guo, E. A. Verploegen, W. Lu, and A. J. Hart, 2009, J. Phys. Chem. C **113**, 20576.

Benedict, L. X., S. G. Louie, and M. L. Cohen, 1996, Solid State Commun. **100**, 177.

Berber, S., Y.-K. Kwon, and D. Tománek, 2000, Phys. Rev. Lett. **84**, 4613.

Bhattacharya, S., R. Amalraj, and S. Mahapatra, 2011, IEEE Electron Device Lett. **32**, 203.

Borca-Tasciuc, T., S. Vafaei, D. A. Borca-Tasciuc, B. Q. Wei, R. Vajtai, and P. M. Ajayan, 2005, J. Appl. Phys. **98**, 054309.

Brenner, D. W., 1990, Phys. Rev. B **42**, 9458.

Brenner, D. W., O. A. Shenderova, J. A. Harrison, S. J. Stuart, B. Ni, and S. B. Sinnott, 2002, J. Phys. Condens. Matter **14**, 783.

Brown, E., L. Hao, J. C. Gallop, and J. C. Macfarlane, 2005, Appl. Phys. Lett. **87**, 023107.

Bui, K., H. Nguyen, C. Cousin, A. Striolo, and D. V. Papavassiliou, 2012, J. Phys. Chem. C **116**, 4449.

Bushmaker, A. W., V. V. Deshpande, M. W. Bockrath, and S. B. Cronin, 2007, Nano Lett. **7**, 3618.

Cahill, D. G., 1990, Rev. Sci. Instrum. **61**, 802.

Cahill, D. G., W. K. Ford, K. E. Goodson, G. D. Mahan, A. Majumdar, H. J. Maris, R. Merlin, and S. R. Phillpot, 2003, J. Appl. Phys. **93**, 793.

Cai, W., A. L. Moore, Y. Zhu, X. Li, S. Chen, L. Shi, and R. S. Ruoff, 2010, Nano Lett. **10**, 1645.

Cao, J. X., X. H. Yan, Y. Xiao, and J. W. Ding, 2004, Phys. Rev. B **69**, 073407.

Casimir, H. B. G., 1938, Physica (Amsterdam) **5**, 495.

Chalopin, Y., S. Volz, and N. Mingo, 2008, arXiv:0809.2660.

Chalopin, Y., S. Volz, and N. Mingo, 2009, J. Appl. Phys. **105**, 084301.

Chang, C. W., D. Okawa, A. Majumdar, and A. Zettl, 2006, Science **314**, 1121.

Chantrenne, P., and J.-L. Barrat, 2004, Superlattices Microstruct. **35**, 173.

Chaudhuri, A., A. Kundu, D. Roy, A. Dhar, J. L. Lebowitz, and H. Spohn, 2010, Phys. Rev. B **81**, 064301.

Che, J., T. Cagin, and W. A. Goddard, III, 2000, Nanotechnology **11**, 65.

Choi, T. Y., D. Poulikakos, J. Tharian, and U. Sennhauser, 2005, Appl. Phys. Lett. **87**, 013103.

Choi, T.-Y., D. Poulikakos, J. Tharian, and U. Sennhauser, 2006, Nano Lett. **6**, 1589.

Chow, W. L., C. C. Yap, D. Tan, M. Shakerzadeh, M. K. Samani, C. Brun, E. H. T. Teo, D. Baillargeat, and B. K. Tay, 2012, in *Microwave Symposium Digest (MTT), 2012 IEEE MTT-S International* (IEEE, New York), pp. 1–3 [DOI: 10.1109/MWSYM.2012.6259415].

Cola, B. A., J. Xu, C. Cheng, X. Xu, T. S. Fisher, and H. Hu, 2007, J. Appl. Phys. **101**, 054313.

Cola, B. A., X. Xu, and T. S. Fisher, 2007, Appl. Phys. Lett. **90**, 093513.

Cola, B. A., X. Xu, T. S. Fisher, M. A. Capano, and P. B. Amama, 2008, Nanoscale Micro. Thermophys. Eng. **12**, 228.

Cross, R., B. A. Cola, T. Fisher, X. Xu, and S. Graham, 2010, Nanotechnology **21**, 445705.

Deshpande, V. V., S. Hsieh, A. W. Bushmaker, M. Bockrath, and S. B. Cronin, 2009, Phys. Rev. Lett. **102**, 105501.

Dresselhaus, M. S., G. Dresselhaus, and P. Avouris, 2001, *Carbon Nanotubes: Synthesis, Structure, Properties, and Applications* (Springer, Berlin/New York).

Dresselhaus, M. S., G. Dresselhaus, J. C. Charlier, and E. Hernãndez, 2004, Phil. Trans. R. Soc. A **362**, 2065.

Dresselhaus, M. S., G. Dresselhaus, and M. Hofmann, 2008, in *Papers from the 2nd International Conference on One-Dimensional Nanostructures* (AVS, Malmo, Sweden), Vol. 26, pp. 1613–1618.

Dresselhaus, M. S., G. Dresselhaus, and A. Jorio, 2004, Annu. Rev. Mater. Res. **34**, 247.

Dresselhaus, M. S., G. Dresselhaus, and R. Saito, 1995, Carbon **33**, 883.

Dresselhaus, M. S., and P. C. Eklund, 2000, Adv. Phys. **49**, 705.

Eletskii, A. V., 2009, Phys. Usp. **52**, 209.

Evans, W. J., M. Shen, and P. Keblinski, 2012, Appl. Phys. Lett. **100**, 261908.

Fischer, J. E., W. Zhou, J. Vavro, M. C. Llaguno, C. Guthy, R. Haggenmueller, M. J. Casavant, D. E. Walters, and R. E. Smalley, 2003, J. Appl. Phys. **93**, 2157.

Fujii, M., X. Zhang, H. Xie, H. Ago, K. Takahashi, T. Ikuta, H. Abe, and T. Shimizu, 2005, Phys. Rev. Lett. **95**, 065502.

Gao, Y., T. Kodama, Y. Won, S. Dogbe, L. Pan, and K. E. Goodson, 2012, Carbon, **50**, 3789.

Gao, Y., A. Marconnet, M. Panzer, S. LeBlanc, S. Dogbe, Y. Ezzahri, A. Shakouri, and K. Goodson, 2010, J. Electron. Mater. **39**, 1456.

Gao, Y., A. M. Marconnet, R. Xiang, S. Maruyama, and K. E. Goodson, 2013, *IEEE Transactions on Components, Packaging and Manufacturing Technology* (IEEE, New York) [DOI: 10.1109/TCPMT.2013.2254175].

Gao, Z. L., K. Zhang, and M. M. F. Yuen, 2011, Nanotechnology **22**, 265611.

Gojny, F. H., M. H. G. Wichmann, B. Fiedler, I. A. Kinloch, W. Bauhofer, A. H. Windle, and K. Schulte, 2006, Polymer **47**, 2036.

Gonnet, P., Z. Liang, E. S. Choi, R. S. Kadambala, C. Zhang, J. S. Brooks, B. Wang, and L. Kramer, 2006, Curr. Appl. Phys. **6**, 119.

Grujicic, M., G. Cao, and B. Gersten, 2004, Mater. Sci. Eng. B **107**, 204.

Grujicic, M., G. Cao, and W. N. Roy, 2005, J. Mater. Sci. **40**, 1943.

Hamdan, A., J. Cho, R. Johnson, J. Jiao, D. Bahr, R. Richards, and C. Richards, 2010, Nanotechnology **21**, 015702.

Heo, Y. J., C. H. Yun, W. N. Kim, and H. S. Lee, 2011, Curr. Appl. Phys. **11**, 1144.

Hodson, S. L., T. Bhuvana, B. A. Cola, X. Xu, G. U. Kulkarni, and T. S. Fisher, 2011, J. Electron. Packag. **133**, 020907.

Hone, J., 2001, in *Carbon Nanotubes, Topics in Applied Physics*, edited by M. S. Dresselhaus, G. Dresselhaus, and P. Avouris (Springer, Berlin/Heidelberg), Vol. 80, pp. 273–286.
Hone, J., 2004, *Dekker Encyclopedia of Nanoscience and Nanotechnology* (Marcel Dekker Inc., New York), pp. 603–610.
Hone, J., B. Batlogg, Z. Benes, A. T. Johnson, and J. E. Fischer, 2000, Science **289**, 1730.
Hone, J., M. C. Llaguno, N. M. Nemes, A. T. Johnson, J. E. Fischer, D. A. Walters, M. J. Casavant, J. Schmidt, and R. E. Smalley, 2000, Appl. Phys. Lett. **77**, 666.
Hone, J., M. Whitney, C. Piskoti, and A. Zettl, 1999, Phys. Rev. B **59**, R2514.
Hsu, I. K., R. Kumar, A. Bushmaker, S. B. Cronin, M. T. Pettes, L. Shi, T. Brintlinger, M. S. Fuhrer, and J. Cumings, 2008, Appl. Phys. Lett. **92**, 063113.
Hu, X. J., A. A. Padilla, J. Xu, T. S. Fisher, and K. E. Goodson, 2006, J. Heat Transfer **128**, 1109.
Huang, X., J. Wang, G. Eres, and X. Wang, 2011, Carbon **49**, 1680.
ITRS, 2011, "International Technology Roadmap for Semiconductors: Interconnect".
Ivanov, I., A. Puretzky, G. Eres, H. Wang, Z. Pan, H. Cui, R. Jin, J. Howe, and D. B. Geohegan, 2006, Appl. Phys. Lett. **89**, 223110.
Jakubinek, M. B., M. A. White, G. Li, C. Jayasinghe, W. Cho, M. J. Schulz, and V. Shanov, 2010, Carbon **48**, 3947.
Javey, A., Q. Wang, A. Ural, Y. Li, and H. Dai, 2002, Nano Lett. **2**, 929.
Jishi, R. A., L. Venkataraman, M. S. Dresselhaus, and G. Dresselhaus, 1993, Chem. Phys. Lett. **209**, 77.
Johnson, R. D., D. F. Bahr, C. D. Richards, R. F. Richards, D. McClain, J. Green, and J. Jiao, 2009, Nanotechnology **20**, 065703.
Josell, D., S. H. Brongersma, and Z. Tkei, 2009, Annu. Rev. Mater. Res. **39**, 231.
Kahaly, M. U., and U. V. Waghmare, 2007, Appl. Phys. Lett. **91**, 023112.
Keblinski, P., and F. Cleri, 2004, Phys. Rev. B **69**, 184201.
Kim, P., L. Shi, A. Majumdar, and P. L. McEuen, 2001, Phys. Rev. Lett. **87**, 215502.
Krumhansl, J. A., and J. A. D. Matthew, 1965, Phys. Rev. **140**, A1812.
Lazzeri, M., S. Piscanec, F. Mauri, A. C. Ferrari, and J. Robertson, 2005, Phys. Rev. Lett. **95**, 236802.
Lee, J. W., A. J. Meade, E. V. Barrera, and J. A. Templeton, 2010, Proceedings of the Institution of Mechanical Engineers, Part N: Journal of Nanoengineering and Nanosystems **224**, 41.
Lepri, S., R. Livi, and A. Politi, 2003, Phys. Rep. **377**, 1.
Li, B., *et al.*, 2010, Adv. Mater. **22**, 3058.
Li, B., T. D. Sullivan, T. C. Lee, and D. Badami, 2004, Microelectronics Reliability **44**, 365.
Li, D., 2002, Ph.D. thesis (University of California, Berkeley).
Li, J., 2000, Ph.D. thesis (Massachusetts Institute of Technology).
Li, Q., C. Liu, X. Wang, and S. Fan, 2009, Nanotechnology **20**, 145702.
Lin, W., J. Shang, W. Gu, and C. P. Wong, 2012, Carbon **50**, 1591.
Lindsay, L., and D. A. Broido, 2010, Phys. Rev. B **81**, 205441.
Lukes, J. R., and H. Zhong, 2007, J. Heat Transfer **129**, 705.
Mahan, G. D., and G. S. Jeon, 2004, Phys. Rev. B **70**, 075405.
Mamalis, A. G., L. O. G. Vogtländer, and A. Markopoulos, 2004, Precis. Eng. **28**, 16.
Marconnet, A. M., N. Yamamoto, M. A. Panzer, B. L. Wardle, and K. E. Goodson, 2011, ACS Nano **5**, 4818.
Maruyama, S., 2002, Physica (Amsterdam) **323B**, 193.
Maruyama, S., 2003, Microscale Therm. Eng. **7**, 41.
Maruyama, S., Y. Igarashi, Y. Taniguchi, and Y. Shibuta, 2004, in *Proceedings of the 1st International Symposium on Micro & Nano Technology* (Pacific Center of Thermal-Fluids Engineering, Hawaii).
Maune, H., H.-Y. Chiu, and M. Bockrath, 2006, Appl. Phys. Lett. **89**, 013103.
McEuen, P. L., M. S. Fuhrer, and P. Hongkun, 2002, IEEE Trans. Nanotechnol. **1**, 78.
Mingo, N., and D. A. Broido, 2005a, Phys. Rev. Lett. **95**, 96105.
Mingo, N., and D. A. Broido, 2005b, Nano Lett. **5**, 1221.
Naeemi, A., R. Sarvari, and J. D. Meindl, 2007, in *Proceedings of the 44th ACM/IEEE Design Automation Conference* (IEEE, New York), pp. 568–573.
Okamoto, A., I. Gunjishima, T. Inoue, M. Akoshima, H. Miyagawa, T. Nakano, T. Baba, M. Tanemura, and G. Oomi, 2011, Carbon **49**, 294.
Ong, Z.-Y., and E. Pop, 2010, Phys. Rev. B **81**, 155408.
Oron-Carl, M., and R. Krupke, 2008, Phys. Rev. Lett. **100**, 127401.
Osman, M. A., and D. Srivastava, 2001, Nanotechnology **12**, 21.
Osman, M. A., and D. Srivastava, 2005, Phys. Rev. B **72**, 125413.
Overney, G., W. Zhong, and D. Tománek, 1993, Z. Phys. D **27**, 93.
Padgett, C. W., and D. W. Brenner, 2004, Nano Lett. **4**, 1051.
Pal, S. K., Y. Son, T. Borca-Tasciuc, D. A. Borca-Tasciuc, S. Kar, R. Vajtai, and P. M. Ajayan, 2008, J. Mater. Res. **23**, 2099.
Panzer, M. A., G. Zhang, D. Mann, X. Hu, E. Pop, H. Dai, and K. E. Goodson, 2008, J. Heat Transfer **130**, 052401.
Panzer, M. A., H. M. Duong, J. Okawa, J. Shiomi, B. L. Wardle, S. Maruyama, and K. E. Goodson, 2010, Nano Lett. **10**, 2395.
Panzer, M. A., and K. E. Goodson, 2008, J. Appl. Phys. **103**, 094301.
Panzer, M. A., and K. E. Goodson, 2011, J. Appl. Phys. **109**, 059902.
Perebeinos, V., S. V. Rotkin, A. G. Petrov, and P. Avouris, 2009, Nano Lett. **9**, 312.
Pettes, M. T., and L. Shi, 2009, Adv. Funct. Mater. **19**, 3918.
Pop, E., 2008, Nanotechnology **19**, 295202.
Pop, E., 2010, Nano Res. **3**, 147.
Pop, E., D. Mann, J. Cao, Q. Wang, K. Goodson, and H. Dai, 2005, Phys. Rev. Lett. **95**, 155505.
Pop, E., D. Mann, Q. Wang, K. E. Goodson, and H. Dai, 2006, Nano Lett. **6**, 96.
Pop, E., D. A. Mann, K. E. Goodson, and H. Dai, 2007, J. Appl. Phys. **101**, 093710.
Popov, V. N., 2002, Phys. Rev. B **66**, 153408.
Popov, V. N., 2004, Carbon **42**, 991.
Popov, V. N., V. E. Van Doren, and M. Balkanski, 2000, Phys. Rev. B **61**, 3078.
Prasher, R., T. Tong, and A. Majumdar, 2007, J. Appl. Phys. **102**, 104310.
Prasher, R. S., X. J. Hu, Y. Chalopin, N. Mingo, K. Lofgreen, S. Volz, F. Cleri, and P. Keblinski, 2009, Phys. Rev. Lett. **102**, 105901.
Qiu, B., Y. Wang, Q. Zhao, and X. Ruan, 2012, Appl. Phys. Lett. **100**, 233104.
Rego, L. G. C., and G. Kirczenow, 1998, Phys. Rev. Lett. **81**, 232.
Ren, Z., Y. Lan, and Y. Wang, 2013, *Aligned Carbon Nanotubes* (Springer, Berlin/Heidelberg), pp. 183–253.
Roberts, N. A., and D. G. Walker, 2011, Int. J. Therm. Sci. **50**, 648.
Rotkin, S. V., V. Perebeinos, A. G. Petrov, and P. Avouris, 2009, Nano Lett. **9**, 1850.
Ruoff, R. S., and D. C. Lorents, 1995, Carbon **33**, 925.

Saito, R., G. Dresselhaus, and M. S. Dresselhaus, 1998, *Physical Properties of Carbon Nanotubes* (Imperial College Press, London).
Saito, R., T. Takeya, T. Kimura, G. Dresselhaus, and M. S. Dresselhaus, 1998, Phys. Rev. B **57**, 4145.
Sánchez-Portal, D., E. Artacho, J. M. Soler, A. Rubio, and P. Ordejón, 1999, Phys. Rev. B **59**, 12 678.
Savić, I., N. Mingo, and D. A. Stewart, 2008, Phys. Rev. Lett. **101**, 165502.
Seol, J. H., *et al.*, 2010, Science **328**, 213.
Sevik, C., H. Sevinçli, G. Cuniberti, and T. Çan, 2011, Nano Lett. **11**, 4971.
Shang, L., L. Ming, and W. Wang, 2007, in *Proceedings of the 7th IEEE Conference on Nanotechnology* (IEEE, New York), pp. 206–210.
Shi, L., D. Li, C. Yu, W. Jang, D. Kim, Z. Yao, P. Kim, and A. Majumdar, 2003, J. Heat Transfer **125**, 881.
Shi, L., J. Zhou, P. Kim, A. Bachtold, A. Majumdar, and P. L. McEuen, 2009, J. Appl. Phys. **105**, 104305.
Sinha, S., and K. E. Goodson, 2005, Int. J. Multiscale Comput. Eng. **3**, 107.
Son, Y., S. K. Pal, T. Borca-Tasciuc, P. M. Ajayan, and R. W. Siegel, 2008, J. Appl. Phys. **103**, 024911.
Steiner, M., M. Freitag, V. Perebeinos, J. C. Tsang, J. P. Small, M. Kinoshita, D. Yuan, J. Liu, and P. Avouris, 2009, Nat. Nanotechnol. **4**, 320.
Stuart, S. J., A. B. Tutein, and J. A. Harrison, 2000, J. Chem. Phys. **112**, 6472.
Takahashi, K., M. Inoue, and Y. Ito, 2010, Jpn. J. Appl. Phys. **49**, 02BD12.
Tans, S. J., A. R. M. Verschueren, and C. Dekker, 1998, Nature (London) **393**, 49.
Tersoff, J., 1988a, Phys. Rev. Lett. **61**, 2879.
Tersoff, J., 1988b, Phys. Rev. B **37**, 6991.
Tersoff, J., 1989, Phys. Rev. B **39**, 5566.
Thostenson, E. T., Z. Ren, and T.-W. Chou, 2001, Compos. Sci. Technol. **61**, 1899.
Tong, T., A. Majumdar, Z. Yang, A. Kashani, L. Delzeit, and M. Meyyappan, 2006, in *Proceedings of the Tenth Intersociety Conference on Thermal and Thermomechanical Phenomena in Electronics Systems (ITHERM '06)* (IEEE, New York), pp. 1406–1411.
Tong, T., Z. Yang, L. Delzeit, A. Kashani, M. Meyyappan, and A. Majumdar, 2007, IEEE Transactions on Components and Packaging Technologies **30**, 92.
Treacy, M. M. J., T. W. Ebbesen, and J. M. Gibson, 1996, Nature (London) **381**, 678.
Turney, J. E., A. J. H. McGaughey, and C. H. Amon, 2009, Phys. Rev. B **79**, 224305.
Varshney, V., S. S. Patnaik, A. K. Roy, and B. L. Farmer, 2010, J. Chem. Phys. C **114**, 16 223.
Varshney, V., S. S. Patnaik, A. K. Roy, G. Froudakis, and B. L. Farmer, 2010, ACS Nano **4**, 1153.
Volkov, A. N., T. Shiga, D. Nicholson, J. Shiomi, and L. V. Zhigilei, 2012, J. Appl. Phys. **111**, 053501.
Volkov, A. N., and L. V. Zhigilei, 2010a, J. Phys. Chem. C **114**, 5513.
Volkov, A. N., and L. V. Zhigilei, 2010b, Phys. Rev. Lett. **104**, 215902.
Volkov, A. N., and L. V. Zhigilei, 2010c, ACS Nano **4**, 6187.
Volkov, A. N., and L. V. Zhigilei, 2012, Appl. Phys. Lett. **101**, 043113.
Wang, J., 2011, Appl. Phys. Lett. **99**, 091905.
Wang, J., and J.-S. Wang, 2006, Appl. Phys. Lett. **88**, 111903.
Wang, X., Z. Zhong, and J. Xu, 2005, J. Appl. Phys. **97**, 064302.
Wang, Z., D. Tang, X. Zheng, W. Zhang, and Y. Zhu, 2007, Nanotechnology **18**, 475714.
Wang, Z. L., D. W. Tang, X. B. Li, X. H. Zheng, W. G. Zhang, L. X. Zheng, Y. T. Zhu, A. Z. Jin, H. F. Yang, and C. Z. Gu, 2007, Appl. Phys. Lett. **91**, 123113.
Wei, B. Q., R. Vajtai, and P. M. Ajayan, 2001, Appl. Phys. Lett. **79**, 1172.
Wei, L., F. Yanhui, P. Jia, and Z. Xinxin, 2012, J. Heat Transfer **134**, 092401.
Won, Y., Y. Gao, M. A. Panzer, S. Dogbe, L. Pan, T. W. Kenny, and K. E. Goodson, 2012, Carbon **50**, 347.
Wu, G., and B. Li, 2008, J. Phys. Condens. Matter **20**, 175211.
Wu, M. C. H., and J.-Y. Hsu, 2009, Nanotechnology **20**, 145401.
Xie, H., A. Cai, and X. Wang, 2007, Phys. Lett. A **369**, 120.
Xie, X., *et al.*, 2012, ACS Nano **6**, 10 267.
Xu, J., and T. S. Fisher, 2006a, IEEE Transactions on Components and Packaging Technologies **29**, 261.
Xu, J., and T. S. Fisher, 2006b, Int. J. Heat Mass Transfer **49**, 1658.
Xu, Y., Y. Zhang, E. Suhir, and X. Wang, 2006, J. Appl. Phys. **100**, 074302.
Yamaguchi, Y., and S. Maruyama, 1998, Chem. Phys. Lett. **286**, 336.
Yamamoto, T., S. Konabe, J. Shiomi, and S. Maruyama, 2009, Appl. Phys. Express **2**, 095003.
Yamamoto, T., K. Sasaoka, and S. Watanabe, 2011, Phys. Rev. Lett. **106**, 215503.
Yamamoto, T., S. Watanabe, and K. Watanabe, 2004a, Thin Solid Films **464–465**, 350.
Yamamoto, T., S. Watanabe, and K. Watanabe, 2004b, Phys. Rev. Lett. **92**, 75502.
Yan, X. H., Y. Xiao, and Z. M. Li, 2006, J. Appl. Phys. **99**, 124304.
Yang, D. J., S. G. Wang, Q. Zhang, P. J. Sellin, and G. Chen, 2004, Phys. Lett. A **329**, 207.
Yang, D. J., Q. Zhang, G. Chen, S. F. Yoon, J. Ahn, S. G. Wang, Q. Zhou, Q. Wang, and J. Q. Li, 2002, Phys. Rev. B **66**, 165440.
Yang, J., S. Waltermire, Y. Chen, A. A. Zinn, T. T. Xu, and D. Li, 2010, Appl. Phys. Lett. **96**, 023103.
Yang, N., G. Zhang, and B. Li, 2008, Appl. Phys. Lett. **93**, 243111.
Yang, N., G. Zhang, and B. Li, 2010, Nano Today **5**, 85.
Yao, Z., J.-S. Wang, B. Li, and G.-R. Liu, 2005, Phys. Rev. B **71**, 085417.
Yu, C., L. Shi, Z. Yao, D. Li, and A. Majumdar, 2005, Nano Lett. **5**, 1842.
Yu, J., R. K. Kalia, and P. Vashishta, 1995, J. Chem. Phys. **103**, 6697.
Zhang, G., and B. Li, 2005, J. Chem. Phys. **123**, 114714.
Zhang, H. L., J. F. Li, K. F. Yao, and L. D. Chen, 2005, J. Appl. Phys. **97**, 114310.
Zhang, H.-L., J.-F. Li, B.-P. Zhang, K.-F. Yao, W.-S. Liu, and H. Wang, 2007, Phys. Rev. B **75**, 205407.
Zhang, K., Y. Chai, M. M. F. Yuen, D. G. W. Xiao, and P. C. H. Chan, 2008, Nanotechnology **19**, 215706.
Zhang, K., H. Fan, and M. M. F. Yuen, 2006, in *Proceedings of the International Conference on Electronic Materials and Packaging* (IEEE, New York), pp. 1–4.
Zhang, K., X. Guo-Wei, C. K. Y. Wong, G. Hong-Wei, M. M. F. Yuen, P. C. H. Chan, and X. Bing, 2005, in *Proceedings of the 55th*

Electronic Components and Technology Conference (IEEE, New York), pp. 60–65.

Zhang, L., Z. Li, Y. Tan, G. Lolli, N. Sakulchaicharoen, F. G. Requejo, B. S. Mun, and D. E. Resasco, 2006, Chem. Mater. **18**, 5624.

Zhang, W., Z. Zhu, F. Wang, T. Wang, L. Wun, and Z. Wang, 2004, Nanotechnology **15**, 936.

Zhang, X., S. Fujiwara, and M. Fujii, 1999, in *Proceedings of the 15th European Conference on Thermophysical Properties* (University of Würzburg, Würzburg, Germany), pp. 477–787.

Zhigilei, L. V., C. Wei, and D. Srivastava, 2005, Phys. Rev. B **71**, 165417.

Zhong, H., and J. R. Lukes, 2004, in *Proceedings of the 2004 ASME International Mechanical Engineering Congress and Exposition* (ASME, New York).

Zhong, H., and J. R. Lukes, 2006, Phys. Rev. B **74**, 125403.